LA-UR-21-25223

Title: SURFplus model calibration for PBX 9012

Author(s):   Menikoff, Ralph

Intended for: Report

Issued: 2021-06-02

SURFplus model calibration for PBX 9012

Ralph Menikoff

May 25, 2021

1 Introduction

PBX 9012 is a plastic bonded explosive composed of 90.2 wt % HMX (cyclo-tetramethylene-tetranitramine) and 9.8 % Viton A (vinylidene–hexafluoropropylene copolymer). It has nearly the same composition as LX-07 (90 % HMX and 10 % Viton A) but with a slightly lower density. Hence it has a higher porosity and is slightly more shock sensitive.

   Here we describe the SURFplus model calibration for PBX 9012 using data from five shock-to-detonation transition (SDT) gas gun experiments by Burns and Chiquete [2020], detonation front shape data from rate stick experiments and cylinder test experiment reported in Anderson et al. [2020], Jackson et al. [2020]. The SDT experiments provide Pop plot data points (run distance-to-detonation) which characterize shock initiation, Lagrangian velocity time histories from embedded magnetic velocity gauges which give information on the reaction behind the lead shock, and Hugoniot data points for the reactants EOS. The rate stick experiments provide data on the curvature effect which characterize propagating detonation waves. The cylinder test experiments provide data on the detonation release isentrope used to calibrate the products EOS. The HE model uses a Davis reactants EOS with parameters that Burns and Chiquete [2020] fit to Hugoniot data, and Davis products EOS with parameters that Anderson et al. [2020] fit to cylinder test data.

   The burn rate calibration is based on comparing experimental data to simulated data. The setup for SDT simulations corresponds to the way in which the HE is initiated in the gas gun experiments. Namely, a projectile with its measured velocity next to the HE. The initial shock pressure corresponds to the value from the shock impedance match of the projectile impacting the HE.

   For any HE model to fit the Pop plot, it is important that the Pop plot data points from each experiment are consistent with the pressure from the impedance match. The Pop plot data points listed in [Burns and Chiquete, 2020] use an initial shock pressure determined from particle and shock velocities inferred from magnetic velocity gauges that are significantly different (compared to estimated uncertainties) from the impedance match shock pressure. Uncertainties in analyzing the data are discussed in the next section. The burn rate calibration adjusts the Pop plot data points to use the shock pressure from the impedance match.

The following sections first discuss the calibrated EOS for the reactants and products, and the calibrated rate. Then the comparison between the experimental and simulated data is presented. The calibration simulations use the Eulerian `xRage` code. Input parameters for `xRage` are listed in the appendices. The comparison utilizes the data files that the experimentalists have contributed to the LANL small-scale database.

2 Embedded gauge diagnostics

Data for shock initiation and the reactant shock locus comes from the SDT experiments with embedded magnetic velocity gauges. The diagnostics [see fig 1, Burns and Chiquete, 2020] include: 1. An accurate measurement (0.1 percent) of the projectile velocity, 2. Stirrup gauge to measure particle velocity time history at the projectile-HE interface, 3. Embedded velocity gauges to measure the particle velocity time history at up to 9 Lagrangian points, 4. Three tracker gauges (left, center and right) to measure (x, t) trajectory points of the lead shock.

In private communications, the experimenters noted that compatibility issues required a different glue than the low viscosity AngstromBond epoxy normally used to obtain thin glue joints between embedded gauge package and the HE. For the PBX 9012 experiments, a silicon glue was used. It is more viscous and can result in glue layers up to 50 microns, which is comparable to the thickness of the gauge package. This raises the question of what effect the relatively thick glue layer have on the gauge response.

2.1 Effect of glue joints

High resolution simulations of the gauge package ($25\,\mu$m teflon + $5\,\mu$m Al + $25\,\mu$m teflon) plus the glue layers and surrounding HE in both 1-D for the stirrup gauge and 2-D for the oblique embedded gauges (typically at a 30 degree angle to the shock front) were reported in [Menikoff, 2021a]. The magnetic gauges measure the particle velocity of the Al conductor.

In 1-D the gauge response shows a rapid rise for the lead shock through the gauge package followed by an equilibration time (due to wave reflections off material interfaces) for the particle velocity of the Al conductor to match the particle velocity of the HE. The lead shock rise time is up to 10 ns due to a small tilt angle (couple of milliradians) when the projectile impacts the HE and also to the gradient of the glue thickness under the active element of the Al conductor [see Menikoff, 2021b]. The equilibration time increases with glue layer thickness. For the 9012 stirrup gauges, the equilibration time is up to 50 ns.

There are additional complications in 2-D. As pointed out by Bdzil [2018], for embedded gauges at an oblique angle to the flow, shear layers form when a shock passes over the material interfaces of the gauge package. This can result in the particle velocity of the Al conductor being a few percent lower than the HE particle velocity. In addition, as the glue layer thickness increases, the downstream perturbations of the flow get larger and extend over a longer time interval. This affects the accuracy to which the particle velocity behind the lead shock can be

determined. The flow perturbations can also affect the reaction rate downstream of the gauge package.

We note there are two glue layers, one on each side of the gauge package. The thickness of the upstream glue layer affects the shock arrival time along the tracker gauges. A spatially varying glue thickness would give varying time offsets between the different tracker gauges.

2.2 Shock speed from fit to tracker gauges

Burns and Chiquete [2020] determined the initial shock pressure and the reactant Hugoniot data points from the particle and shock velocities using the shock relation $P_s = \rho_0 u_p U_s$. The particle velocity is obtained from the jump-off of the velocity gauges, and the shock velocity is derived from a fit to the tracker gauge data for the lead shock trajectory, $x(t)$. The fit smooths the data and enables the derivative $U_s(t) = \mathrm{d}x/\mathrm{d}t$ to be determined free of high frequency noise.

The trajectory fit utilizes a method developed by Hill and Gustavsen [2002]. It is based on integrating a fitting form for the shock acceleration, $\mathrm{d}U_s/\mathrm{d}t$.

$$\frac{\mathrm{d}}{\mathrm{d}t}\begin{pmatrix} x \\ U_s \end{pmatrix} = \begin{pmatrix} U_s \\ a_m \frac{D-U_s}{D-U_m} \exp\left(\frac{U_s-U_m}{D-U_m}\right) \end{pmatrix} \ , \tag{1}$$

where U_s is the shock speed, and the fitting form parameters are the final shock speed D, the shock speed at maximum acceleration U_m and the maximum acceleration a_m. There are also two parameters for the initial conditions of the ODEs; $x_0 = x(t_0)$ and $u_s = U_s(t_0)$. The fitting form works well when the trajectory data has a small scatter as seen in [Hill and Gustavsen, 2002, fig 4 and 5]. It is also used to determine the shock-to-detonation transition point for the Pop plot.

Burns and Chiquete [2020] ODE fits used the combined data from all the tracker gauges, except for shot 1s-1684 for which no data was obtained for the left and right trackers. Their error analyse assumed that the uncertainty of each data point is random and independent. Except for the neighborhood of the transition point, it gave an uncertainty in the shock speed of less than 2 percent [Burns and Chiquete, 2020, fig 9].

The ODE fits to the tracker data are shown in Appendix B. The following features in the data indicate that there are also systematic errors in the tracker data points and that the derived uncertainty in the shock speed is too low.

1. The fits using all the trackers (see fig. 18) show systematic non-constant variations in the residual of each tracker gauge and between different trackers. The slopes of the residual of a tracker gauge (which requires correlations between quite a few adjacent data points and would be improbable if the uncertainty of each data point is independent) implies a difference in the shock speed between the fit and a tracker gauge over an extended time interval.

3

2. The final detonation speed (parameter D) for shot 1s-1674 is 14 percent greater than D_{cj}, which is unreasonably large. It is due to the spatial offset at fixed time of the center tracker compared to the left and right trackers. Leaving out the center gauge, the root mean squared (RMS) residual of the fit is reduced by a factor of 3 (from 147 to $50\,\mu\text{m}$), the final detonation speed is 2.2 percent below D_{cj}, the distance-to-detonation is reduced by $1\,\text{mm}$, and the initial shock speed (parameter $U_s(0)$) increases by 9 percent; see fig. 24 and Table 6.

3. The different tracker gauges can be thought of as redundant measurements of the lead shock trajectory. Separate fits to the left and right tracker data for shot 2s-1101 have comparable RMS residuals but the shock speed is significantly different; see fig. 20. In particular, for the left tracker, $U_s(t)$ displays a more abrupt transition to detonation, similar to the ODE fits of the other shots. The steep transition is physically expected since the reaction rate becomes very large, and is needed for the transition point to be insensitive to the transition criterion.

4. Most fitting routines give the statistical uncertainty σ for each fitting parameter holding the other parameters fixed. However, larger correlated changes to the fitting parameter can give relatively small changes to the RMS residual; see Press et al. [1986, sec. 14.5] for a discussion of the covariance matrix of a least squared fit. An example of this for shot 2s-1101 with all the trackers are ODE fits with D set to D_{cj} compared to D as a free parameter; see fig. 22 and Table 5. The difference between D and D_{CJ} is $7.4\,\sigma_D$, which would be improbable if D is a independent Gausian random variable. The figure shows a small difference in the trajectory $x(t)$ and a significant difference in the $U_s(t)$; in particular an 8 percent increase in the initial shock speed. Consequently, the uncertainty in a particular parameter can be quite a bit larger than than those listed in [Burns and Chiquete, 2020, table VI].

3 EOS model

The SURFplus PBX 9012 model uses a Davis reactants EOS fit to shock data from the SDT experiments, and a Davis products EOS fit to cylinder test data. These are described next.

3.1 Reactants EOS

Reactants shock data points are inferred from the SDT gas gun experiments. Burns and Chiquete [2020, table V] data points are determined by the particle velocity from the jump-off of the stirrup and embedded velocity gauges and the shock speed at the gauge position obtained from the fit to the tracker gauges (discussed in previous section). The shock state is then completely determined by the shock jump conditions; $P_s = \rho_0\, u_p\, u_s$, $V_s = (1 - u_p/u_s)V_0$ and $e_s = \frac{1}{2}(P_s + P_0)(V_0 - V_s)$.

The data points with error bars and their Davis reactants EOS fit to the shock locus [Burns and Chiquete, 2020, sec IV] are shown in fig. 1. We note that the EOS fit is constrained by
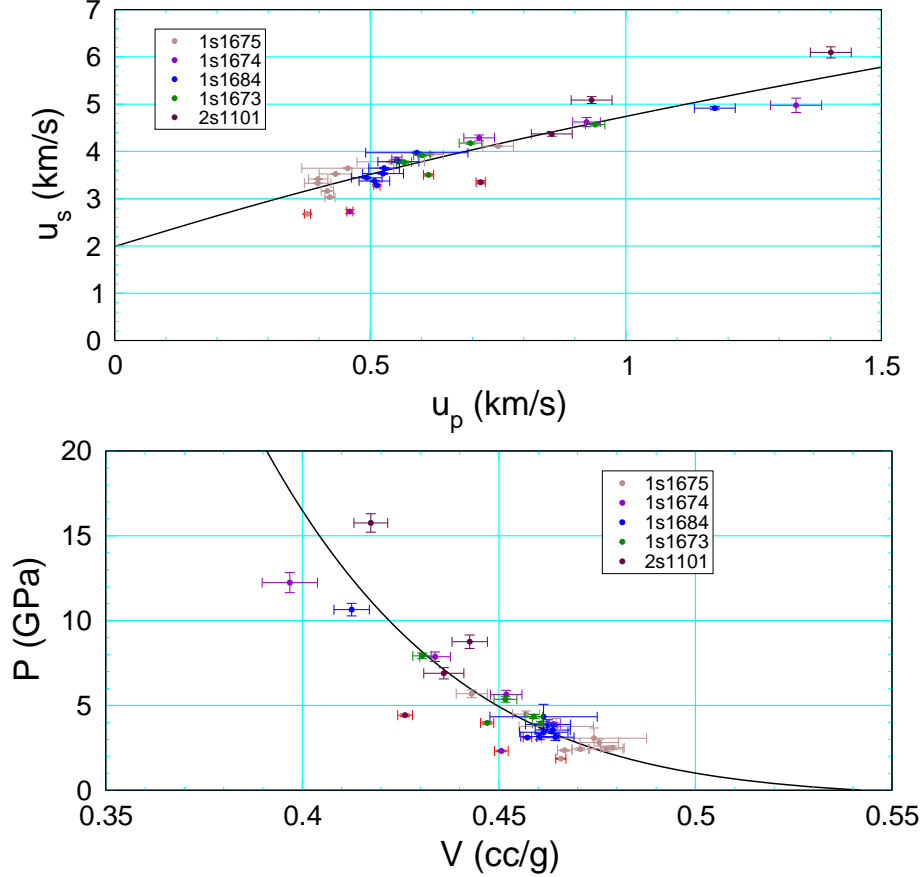
Figure 1: Reactants EOS data points and Davis reactants EOS fit from Burns and Chiquete [2020, table V and table IX]. Data points are color coded by experiment with red error bars for initial shock.

the measured sound speed $c_0 = 1.99\,\mathrm{km/s}$; *i.e.*, $u_s = c_0$ at $u_p = 0$. The error bars on the particle velocity are due to the rise time, shape and noise of the gauge particle velocity time histories. The error bars on the shock speed are based on an analysis of fits to the tracker data assuming independent Gaussian random errors for each data points; see Burns and Chiquete [2020, sec III.E and table VI]. The discussion in the previous section and Appendix B indicates that there are also systematic errors and correlations which lead to larger uncertainties in the shock speed.

One feature in the data plot that stands out is the error bars on the initial shock for each experiment are small yet the data points lie significantly below the EOS fit in both the (u_p, u_s) plane and (V, P)–plane. Since the initial shock drives the SDT, its strength is important for calibrating the reaction rate. Next we consider an alternative means of determining the initial shock strength.

The experiments also measure the projectile speed much more accurately (0.1 percent) than can be obtained for either u_p or u_s. Moreover, parameters for the EOS of the projectile materials (sapphire or Kel-F) have previously been determined; see [Burns and Chiquete, 2020, table III]. Consequently, the initial shock strength can be determined from a shock impedance match, assuming that the derived PBX 9012 reactant EOS is reasonably accurate. This is also how the

initial shock strength in a calibration simulation is set; *i.e.*, a simulation mimics the experiment and starts with the projectile at its measure speed adjacent to the PBX. Hence it is important for consistency between the initial shock strengths reported for Pop plot data points of a series of SDT experiments and the initial shock strengths in the corresponding calibration simulations. The consistency is also important for application simulations since the same EOS model of the HE is used.

The initial values of the particle velocity (see fig. 17), shock speed (see fig. 18) and pressure for each of the 5 SDT experiments are listed in Table 1, along with the reactants shock values from the impedance match with the projectile. Both initial shock states are plotted in fig. 2. It can be seen that the difference in shock speed (up to 20 %) is much larger than the difference in particle velocity (up to 6 %). Both velocity differences are significantly larger than the error bars.

The graphical solution to the impedance match for shots 1s-1674 and 1s-1684 are shown in fig. 3. It can be seen that the match pressure corresponds to the value of the point on the projectile shock locus with a particle velocity of $\Delta u = u_{proj} - u_p$. This provides a check on the initial particle velocity and shock speed that does not depend on the assumed reactants EOS used for the impedance match. The values of u_p and u_s in Burns and Chiquete [2020, table IV]

Table 1: Initial shock state inferred from data for each PBX 9012 experiment and from impedance match with projectile. The 1s shots used a sapphire projectile and the 2s shot used a Kel-F projectile.

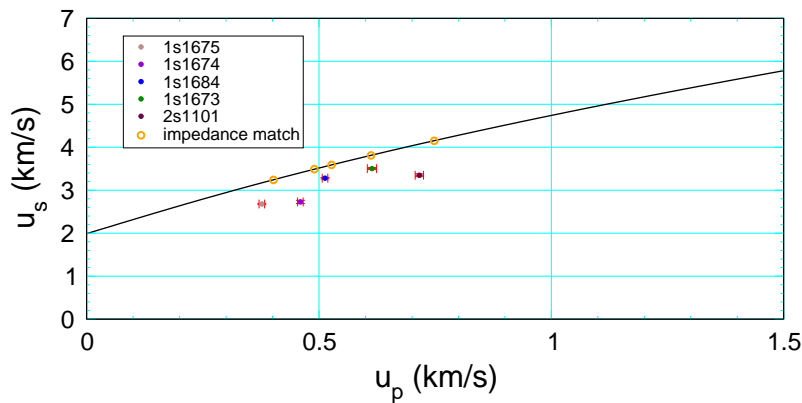| shot	Burns and Chiquete [2020, table IV]				impedance match				ΔP_s (%)
	u_{proj}	u_p	P_s	u_s	$u_{\mathrm{proj}} - u_{p,BC}$	u_p	P_s	u_s	
1s-1675	0.456	0.377	1.86	2.68	0.079	0.402	2.41	3.24	23
1s-1674	0.560	0.460	2.32	2.73	0.100	0.490	3.15	3.49	27
1s-1684	0.605	0.513	3.10	3.28	0.092	0.527	3.49	3.59	11
1s-1673	0.708	0.614	3.97	3.50	0.094	0.612	4.31	3.81	8
2s-1101	1.555	0.716	4.43	3.35	0.839	0.748	5.73	4.15	23

Figure 2: Reactants shock locus (black curve) and initial shock states inferred from data for each PBX 9012 experiment and from impedance match with projectile.
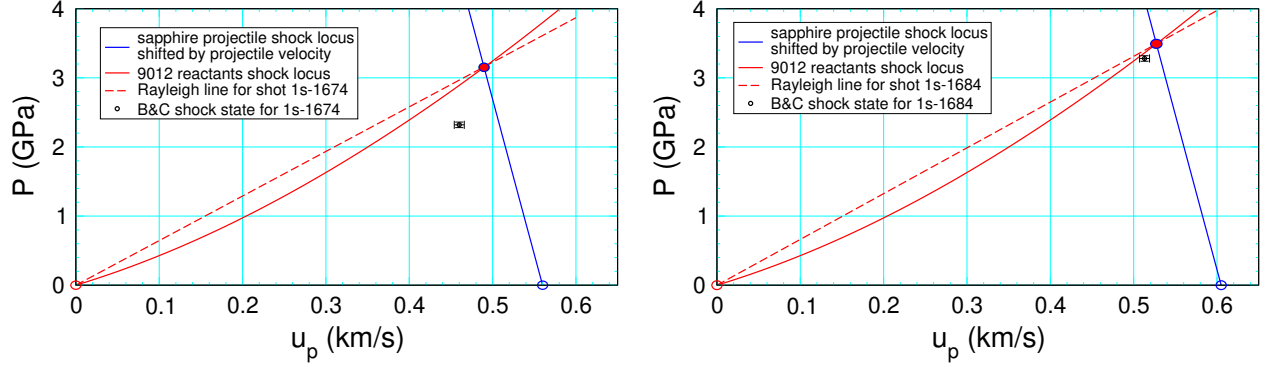
Figure 3: Shock impedance matches for shots 1s-1674 and 1s-1684.

for shot 1s-1674 miss the projectile locus by considerably more than the error bars. Variations in the ODE fits for this shot shown in fig. 24 have values of u_s between 2.7 and 3.0 km/s; see Table 6. But even this would only partly accounts for the discrepancy.

In addition to the inconsistency with the impedance match, there are 2 additional anomalies with the initial shock data points derived from Burns and Chiquete methodology. First, u_s is not monotonic with P_s. Second, for the sapphire projectile shots, Δu is not monotonic with P_s. These anomalies are significant because monotonicity is a general property of shock loci independent of the EOS model. They imply that the uncertainty in the initial shock state must be larger than the estimates.

The pressure difference between the two methods for inferring the initial shock state is large, 8 to 27 percent and affects the Pop plot. In addition, the difference in particle velocity between the stirrup gauge and the impedance match is up to 6 %, see fig. 17. It would be worthwhile to have additional experiments to accurately determine the shock locus in the range of the initial shock pressures of the 5 SDT shots.

3.2   Products EOS

The PBX 9012 model uses a Davis model for the products EOS. The EOS is calibrated to the wall velocity of a cylinder test experiment [Jackson et al., 2020]. The calibrated parameters are from [Anderson et al., 2020, table 6].

To check the calibration, an xRage simulation was run of the experiment (shot # 8-2172). As can be seen in fig. 4, the experimental and simulated wall velocity match very well. We note that the simulated wall velocity is dominated by the products EOS and is insensitive to the burn rate. The axial detonation speed is also measured. It is determined by the curvature effect and depends on the model burn rate. The curvature effect is discussed in a later section.

We note that the ringing in the wall velocity is due to the strength model for the copper wall. The local peaks in the wall velocity are consistently high. This would result in the simulated trajectory of the wall, $r(t)$, getting ahead of the experimental trajectory by a growing
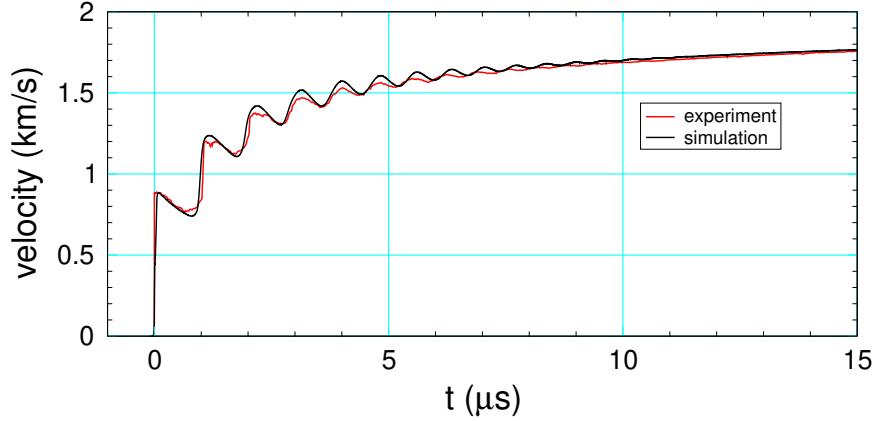
7

Figure 4: Cylinder test wall velocity for PBX 9012 from experiment and xRage simulations with SURFplus model.

amount; *i.e.*, the effect of the excess velocity is cumulative on the position. The difference in the experimental and simulated wall position time histories could be a sensitive measure of accuracy than the wall velocity.

We note that the Davis products EOS is of the Mie-Grüeisen form with the CJ release isentrope as the reference curve. The cylinder test provides data for the release isentrope behind the detonation wave front. There is no overdriven detonation wave data nor data off the CJ release isentrope. Both the pressure regime above the CJ pressure and off the reference isentrope rely on extrapolating the fitting form beyond the available data.

3.3 CJ state and HE loci

The CJ detonation wave states based on the model EOS for initial density 1.845 g/cc is listed below:

```
Initial reactants state
 5.4201e-01  0.0000e+00  0.0000e+00  1.0000e-04  1.9900e+00  1.9900e+00  6.6097e+00  2.9700e+02
VN spike state
 3.4309e-01  4.9899e+00  3.1591e+00  5.0172e+01  8.6080e+00  9.5615e+00  2.2056e+00  1.6986e+03
-----------------------------------------------------------------------------------------------
      V           e           u           P           us          c           FD          T
    cm^3/g       MJ/kg       km/s        GPa         km/s        km/s                    K
-----------------------------------------------------------------------------------------------
CJ products state
 4.0767e-01  2.2757e+00  2.1334e+00  3.3882e+01  8.6080e+00  6.4746e+00  2.0297e+00  3.6849e+03
```

The CJ pressure and detonation speed are a little lower than for PBX 9501. This is as expected since PBX 9012 has more binder than PBX 9501.

The shock locus, detonation locus and the CJ release isentrope are shown in fig. 5. We note that the detonation and shock loci cross at a pressure of about 80 GPa. This is due
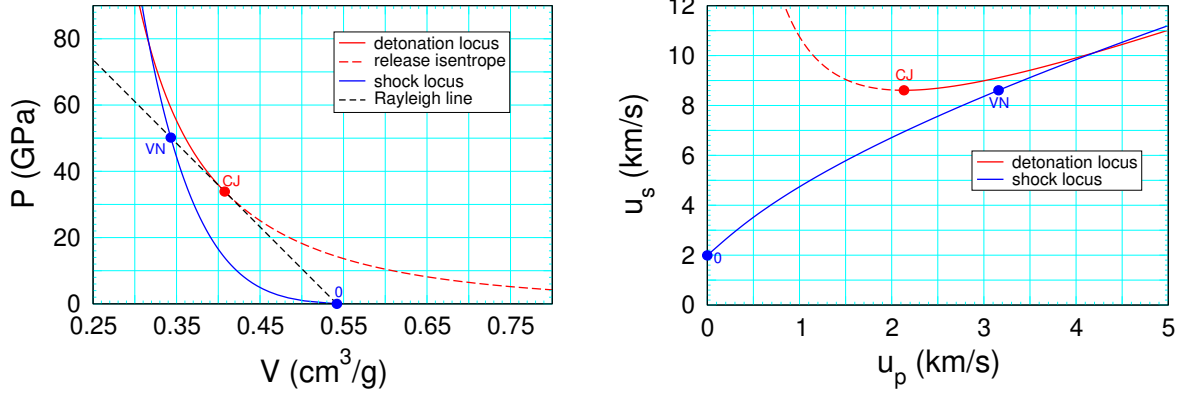
8

Figure 5: Shock and detonation loci for PBX 9012 from model EOS; (V, P)–plane on left and (u_p, u_s)–plane on right.

to extrapolating the reactants and products EOS calibration beyond the data. The crossing pressure is sufficiently above the VN spike state that the reactants would likely be burned and not affect almost all model simulations.

The `xRage` input parameters for the 9012 EOS model are listed in Appendix C.

4   SURFplus rate and ZND profile

The SURF burn rate has the form

$$\lambda = g(s) , \tag{2a}$$

$$\frac{\mathrm{d}}{\mathrm{d}t}s = \tilde{\mathcal{R}}(p_s, p) = f(p_s) \cdot \begin{cases} 0 , & \text{for} \quad p \le 0 \\ \left[\frac{p}{p_s}\right]^n , & \text{for } 0 < p < p_s , \\ \left[\frac{p}{p_s}\right]^{n_{hi}} , & \text{for } p_s \le p \end{cases} \tag{2b}$$

where λ is the SURF reaction progress variable (mass fraction of products), s is a scaled reaction variable, p_s is the lead shock pressure and p is the local pressure. The fitting form for $f(p_s)$ and the SURFplus extension parameters are specified in the xRage users manual and [Menikoff, 2017, App. A and B]. The standard burn rate is $\mathrm{d}\lambda/\mathrm{d}t = (\mathrm{d}g/\mathrm{d}s) \cdot \tilde{\mathcal{R}}(p_s, p)$ where $\mathrm{d}g/\mathrm{d}s$ depends only on λ since $g(s)$ is monotonic and hence invertible.

At low pressures, the SURF rate function $f(P_s)$ is calibrated to Pop plot data. In addition, the low pressure rate cutoff is fit to embedded gauge data for the lowest initial shock pressure SDT experiment. The parameter n_{hi} affects the shape of the embedded gauge velocity time histories and the calibration to Pop plot data. The parameter n affects shock initiation with a pressure decreasing gradient behind the shock front and also the reaction-zone width. The PBX 9012 calibration uses $n = 1.2$ and $n_{hi} = 1.2$.

9

The SURF rate parameters at high pressure and the SURFplus parameters are fit to curvature effect data for the detonation speed as a function of front curvature, $D_n(\kappa)$. It is discussed in detail in a later section. For now we note that a fast and slow reaction rate is needed to fit the shape of the $D_n(\kappa)$ curve. The 9012 model uses SURFplus for the slow rate even though it was developed for the carbon clustering reaction of TATB. The calibrated PBX 9012 function $f(p_s)$ for the SURF rate and the SURFplus rate functions are shown in fig. 6 for the `xRage` input parameters listed in Appendix D.

Compared to the SURFplus parameters for the TATB based PBX 9502, the PBX 9012 model slow reaction has a much smaller energy release of $0.225\,\mathrm{MJ/kg}$. Moreover, after only $22\,\mathrm{ns}$, the slow rate reaction progress variable is $\lambda_2 = 0.32$, and the reaction energy left is down to $0.05\,\mathrm{MJ/kg}$. Consequently, as will be seen later in the SDT simulations, after the transition to detonation, the detonation speed approaches within 0.1 percent of D_{cj} very quickly (sub μs).

The reaction zone or ZND pressure profile versus distance and time for a planar CJ detonation wave are shown in fig. 7. The fast rate has reaction-zone width of $0.077\,\mathrm{mm}$ and reaction time of $0.013\,\mu\mathrm{s}$. The slow rate extends the reaction-zone width to $0.74\,\mathrm{mm}$ and the reaction time to $0.12\,\mu\mathrm{s}$. However, as noted above, most of the slow energy release occurs much sooner.

A complication is that the SURF rate, extrapolated from the ignition regime to the propagating detonation wave regime, needs to be about a factor of 2 larger to fit the curvature effect data for large curvature. The SURF fitting form has parameters to cut off the rate at high pressures, but not to increase the rate. Instead the SURF model has been modified for a partly resolved
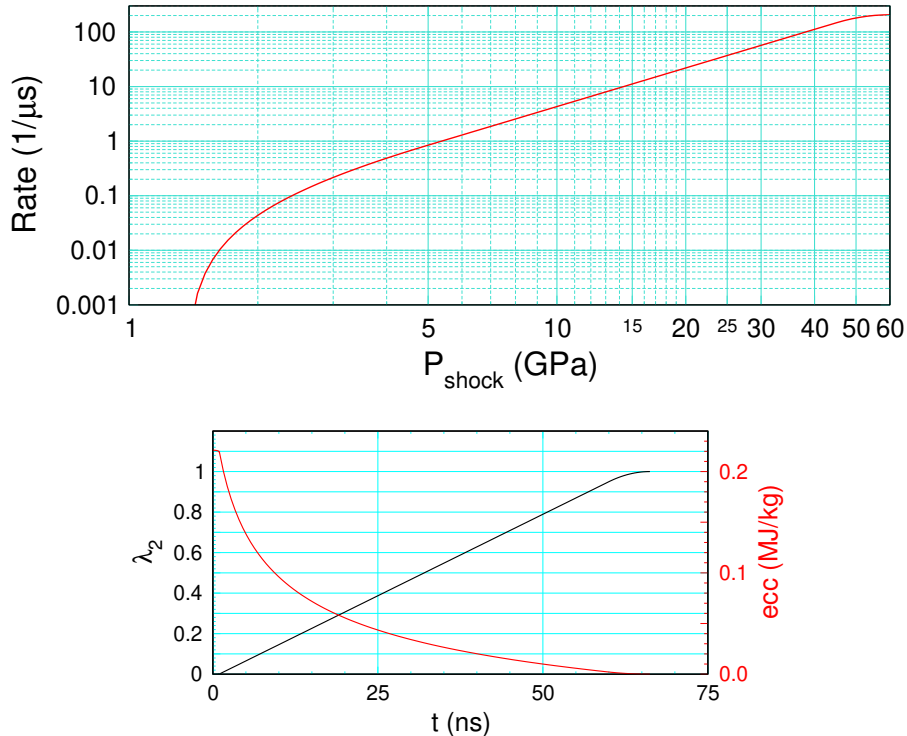

Figure 6: Fast SURF rate function $f(p_s)$ and slow SURFplus rate for PBX 9012.
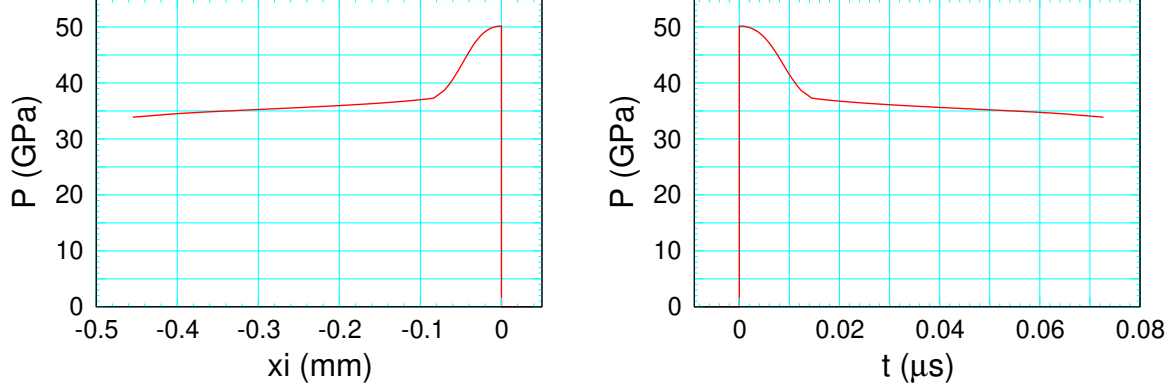
10

Figure 7: CJ detonation wave profiles for SURFplus model of PBX 9012. Pressure vs distance at fixed time on left, and Lagrangian pressure time history on right.

reaction-zone by allowing a controlled amount of burn in the lead shock rise. This has the affect of decreasing the reaction-zone width of a propagating detonation wave and enables the model to fit the curvature effect. The motivation and implementation of the partly resolved reaction-zone is described in Appendix E.

5   Pop plot

Two corrections are made to the PBX 9012 Pop plot data points inferred by Burns and Chiquete [2020, table VIII] from their SDT experiments. First, as discussed in reactants EOS section, the initial shock pressure for each experiment is replace with the pressure from the impedance match for the projectile impact on the HE; see Table 1 and fig. 2. This is needed for the for the Pop plot data and calibration simulations for the series of SDT experiments to be consistent with the model EOS. Second, the run distance and time to detonation is modified for experiments in which the transition point from the shock trajectory analysis is inconsistent with when the embedded velocity gauges profiles show a detonation wave has occurred; *i.e.*, trajectory transition point is clearly downstream of when a velocity gauge shows a detonation wave occurred. This affects 2 shots; 1s-1674 and 2s-1101.

The velocity gauge time histories and lead shock trajectory for the two shots are shown in fig. 8 and fig. 9. The signature of a detonation wave in the gauge time history is a shock rise to a peak velocity greater than the CJ particle velocity (2.1 km/s, see subsection 3.3) followed by a rapid monotonic decrease to some value below the CJ velocity. The first gauge showing a detonation wave and the transition point determined from trajectory analysis are indicated in the figures. For these cases the transition point is taken as the as the shock arrival at the position of the gauge showing a detonation wave.

An anomaly in the shock trajectory for shot 1s-1674 is seen in fig. 8. Before the transition to detonation the time differences among points for the tracker gauges and the lead shock of the velocity gauges are within 0.01 μs. After the transition the velocity gauge and center tracker

Figure 8: Velocity gauge and tracker gauge data for shot 1s-1674 from Burns and Chiquete [2020]. Tracker plot is zoomed in to the neighborhood of the transition point [Burns and Chiquete, 2020, table IV] shown by red diamond. Solid and dashed red lines with arrow marks position of transition from velocity gauge and trajectory analysis, respectively. Blue and magenta guide lines have the slope of the initial shock and detonation wave, respectively.
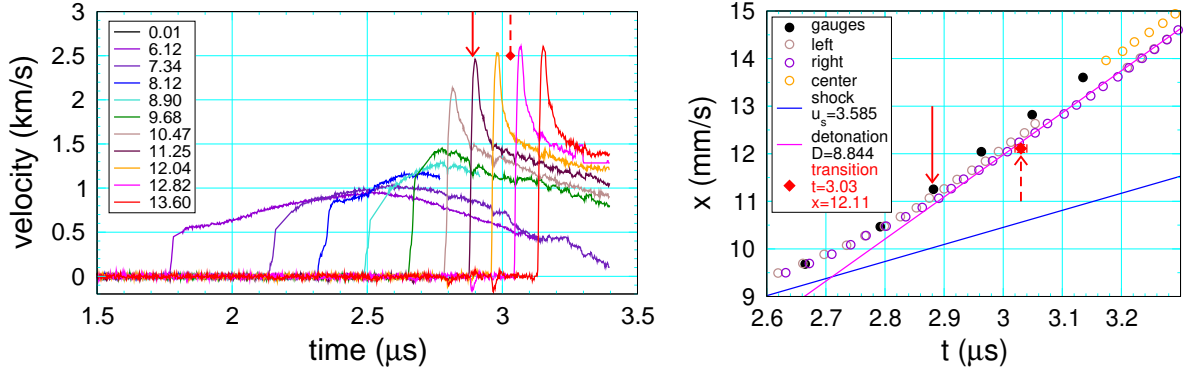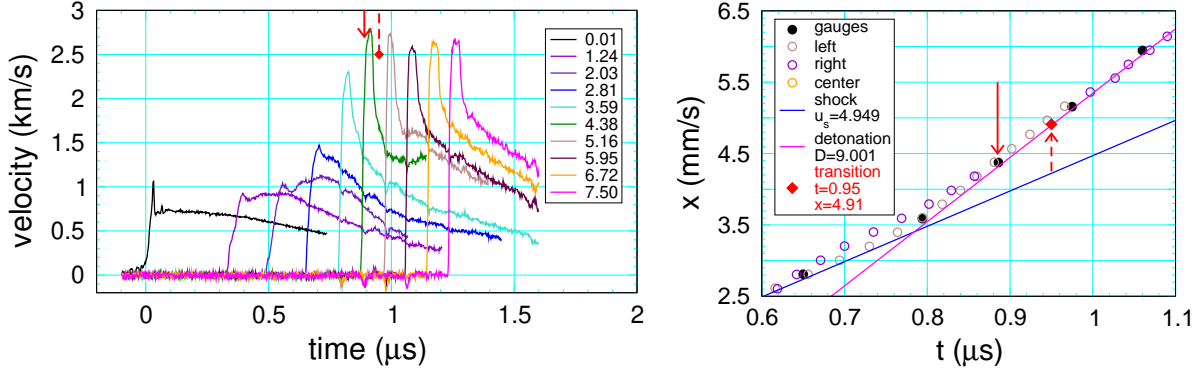

Figure 9: Velocity gauge and tracker gauge data for shot 2s-1101 from Burns and Chiquete [2020]. Tracker plot is zoomed in to the neighborhood of the transition point [Burns and Chiquete, 2020, table IV] shown by red diamond. Solid and dashed red lines with arrow marks position of transition from velocity gauge and trajectory analysis, respectively. Blue and magenta guide lines have the slope of the initial shock and detonation wave, respectively.

are earlier than the left and right trackers by $0.04\,\mu$s. Moreover, for a simple tilt of the shock front, one would expect the time for the trajectory points from the inner (center) tracker to lie between the times for the outer (left and right) trackers. The time offset in the center tracker significantly affects the trajectory fit as shown in fig. 24 and Table 6. With all the tracker gauges, the final detonation speed (fitting parameter D) is 14 percent higher than D_{cj}, which is unreasonably large. The trajectory fit without the center tracker has a transition point $1\,$mm earlier (consistent with velocity gauge data), a detonation speed 2.2 percent lower than D_{cj} and a RMS residual 1/3 less than the fit with the center gauge.

The trajectory fit to shot 2s-1101 also has an anomaly. As seen in fig. 18 the shock speed $u_s(t)$ at the transition is not as abrupt as for the other shots. Consequently, the transition point is sensitive to the transition criterion. A tracker fit with the parameter D fixed at D_{cj} is shown fig. 22. By eye the difference in the $x(t)$ is barely visible, though the RMS residual is 40 percent

larger. However, the transition in the shock speed $u_s(t)$ is more abrupt and the transition point close to the corrected transition point.

The lowest pressure shot 1s-1675 is unusual. The shock speed $u_s(t)$ shown in fig. 18 is qualitatively similar to the other shots. However, the final velocity (parameter D) is 34 percent less than D_{cj}, but constant for the last $0.6\,\mu$s. The final constant shock speed is an artifact of the fitting form for the shock acceleration, which goes to 0 and hence forces the shock speed to a constant at late time. Figure 19 shows that the local average shock speed has a local maximum of $5.48\,$km/s at x=17 mm followed by a gap in the data for $19.7 < x < 21.5$ and then a final value of $5.76\,$km/s at $x = 22$. It is not clear what would cause this anomalous behavior. But in any case, the shock did not transit to a detonation wave within the range of the tracker data.

The original and revised Pop plot data points are listed in Table 2, and plotted in fig. 10. The fit to the revised PBX 9012 data points (excluding shot 1s-1675 which did not transit to a detonation) are

Distance of run: $\quad \log_{10}(x/\mathrm{mm}) = 1.795 - 1.541\,\log_{10}(P/\mathrm{GPa}), \quad$ rel error $4.7\,\%$

Time to detonation: $\quad \log_{10}(t/\mu\mathrm{s}) \quad = 1.424 - 1.952\,\log_{10}(P/\mathrm{GPa}), \quad$ rel error $2.7\,\%$

These Pop plot parameters are used in the calibration of the model burn rate.

For comparison, the LX-07 Pop plot data points and PBX 9501 Pop plot are also shown. The revised PBX 9012 Pop plot is a little more sensitive (smaller run distance and shorter detonation

Table 2: Pop plot data points for PBX 9012 derived from experiments of Burns and Chiquete [2020].

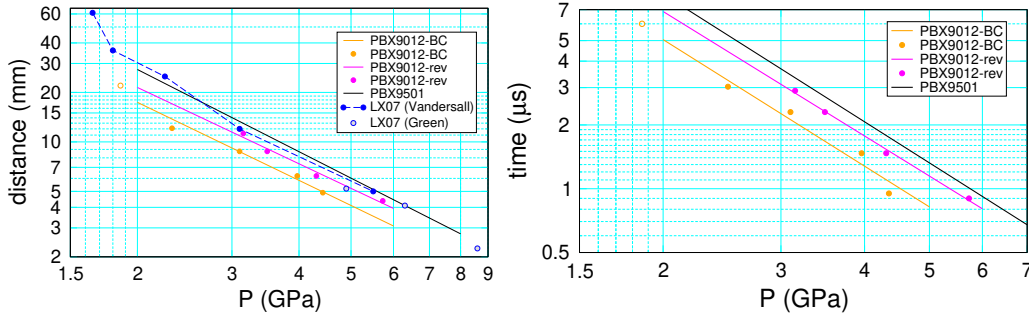| shot	Burns and Chiquete [2020, table VIII]			revised		
	P (GPa)	x (mm)	t (μs)	P (GPa)	x (mm)	t (μs)
1s-1675	1.86	> 22	> 6	2.41	?	?
1s-1674	2.32	12.11	3.03	3.15	11.25	2.88
1s-1684	3.10	8.76	2.30	3.49	8.76	2.30
1s-1673	3.97	6.21	1.47	4.31	6.21	1.47
2s-1101	4.43	4.91	0.95	5.73	4.38	0.89

Figure 10: Pop plot for HMX based PBX 9012, LX-07 and PBX 9501. Solid lines are fit to data points. Solid circles are data points. Open orange circle is listed as lower limit in Table 2. LX-07 data from Vandersall et al. [2010, table II] and Green et al. [1970, table 2].

time for a given shock pressure) than either PBX 9501 or LX-07. The PBX 9012 Pop plot of Burns and Chiquete is significantly more sensitive. It is interesting to note that if a transition were to occur for lowest pressure shot 1s-1675, it would be above the revised Pop plot, and would be similar to the low pressure data points for LX-07.

5.1 Porosity

The relative sensitivities of PBX 9012, LX-07 and PBX 9501 depend largely on the porosity. In general, a larger porosity increases the hotspot burn rate and increases shock sensitivity, while a higher mass fraction of binder decreases the burn rate and shock sensitivity. The porosity is determined from the density and composition; $\phi = 1 - \rho/\rho_{TMD}$, where the theoretical maximum density is $\rho_{TMD} = \lambda_{HE}\rho_{HE} + \lambda_{binder}\rho_{binder}$ and λ is the mass fraction. For PBX 9012, $\rho_{hmx} = 1.90\,\text{g/cc}$, $\rho_{viton} = 1.820\,\text{g/cc}$, $\lambda_{HE} = 0.902$ and $\lambda_{binder} = 0.098$ gives $\rho_{TMD} = 1.892\,\text{g/cc}$. At a density of $1.845\,\text{g/cc}$ the porosity is 2.5 percent.

For LX-07, Vandersall et al. [2010, table I] lists the density as $1.85\,\text{g/cc}$ and Green et al. [1970, table 2] lists the LX-07-02 density as $1.860\,\text{g/cc}$. The resulting porosities are 2.2 and 1.7 percent, respectively. Thus, PBX 9012 is expected to be more shock sensitive than LX-07. However, other values for the density of LX-07 can be found in the literature, ranging from 1.835 to $1.865\,\text{g/cc}$ for which the porosity would vary from 3.2 to 1.4 percent, and may change the relative sensitivity.

PBX 9501 has a higher weight percent HMX than PBX 9012 and a different binder (2.5 % estane and 2.5 % eutectic BDNPA/BDNPF). Its TMD is $1.860\,\text{g/cc}$ [Gibbs and Popolato, 1980, §4.2]. At a density of 1.836, the porosity is 1.3 percent. The Pop plots in fig. 10 show that PBX 9501 has about the same sensitivity as LX-07 and is less sensitive than PBX 9012.

6   Embedded velocity and tracker gauge data

Calibration of the burn rate is an iterative process. The SURF rate parameters n, n_{hi} are adjusted for the shape of the embedded velocity gauge time histories. The cutoff parameters P_1 and P_{high} are adjusted for the reaction-zone width needed for the curvature effect as discussed in the next section. To cover a wide range of pressure for shock initiation, the SURF burn rate parameters C and f_n are chosen to fit the Pop plot. The low pressure cutoff parameters P_0 and P_{low} were adjusted for the lowest pressure shot 1s-1675 that did not transit to a detonation.

As a check on the model, the velocity gauge time histories and lead shock trajectory from the tracker gauges are compared with simulations for all 5 SDT experiments in the next subsections. The shots are ordered by increasing initial shock pressure.

First a few general comments:

1. The SDT simulations are 1-D and neglect perturbations due to the gauges; see [Menikoff, 2021a]. They start with the projectile at its measured velocity adjacent to the HE. Hence, the initial HE shock pressure results from the impedance match of the projectile impacting the HE. The projectile is long enough to sustain the pressure at the projectile/HE interface. The interface velocity decreases as the HE burns and raises the pressure. The simulations used the adaptive mesh refinement capability of the xRage code, with a cell size down to $12\,\mu$m in the reaction zone.

2. Nominally, the time origin for the gauge data corresponds to the lead shock at the front surface of the HE. Experimental it is determined by the stirrup gauge. There is an uncertainty due to the width of the gauge shock profile and the thickness of the glue layers between the gauges and the HE; see fig. 17 for plots of the stirrup gauge profiles and sec. 2.1. The simulated shock trajectory data is from the shock detector of the SURF model. The time origin of the simulation is slightly shifted (0.02 to $0.12\,\mu$s) to account for uncertainty in the time origin and to better match the experimental data.

3. Due to limited temporal response time of the velocity gauges, for a detonation wave the peak velocity is always less than the VN spike velocity based on the EOS; see sec. 3.3. The peak simulated velocity is also less than the VN spike velocity due to the partially resolved reaction-zone model.

4. At the transition to detonation, the simulations show that the detonation speed slightly overshoots D_{cj} and then after a few mm (or equivalently a few tenths of μs) is nearly D_{cj}. This is due to the short reaction time for the fast rate and the release of most of the energy for the slow rate within 25 ns. Consequently, the detonation wave travels many times the effective reaction-zone width, and after a few 100 ns the detonation speed decays to within 0.1 percent of D_{cj}.

5. The ODE fits to the experimental tracker data (see fig. 18 and Table 3) show that the two highest pressure shots have a detonation speed 4 percent above D_{cj} after the transition by over $0.5\,\mu$s and 5 mm. The trajectory data also shows that the different tracker gauges have variable offsets in position at fixed time, possibly from variations in glue thickness around the gauge package. This can affect the shape of the detonation front (*e.g.*, the offsets imply the front of shot 1s-1674 is bowed out at the center) and the detonation speed inferred from the different gauges.

6. When the experimental and simulated detonation speed differ, the comparison of the lead shock trajectories shows a noticeable difference at late time since the slopes of the trajectory differ.
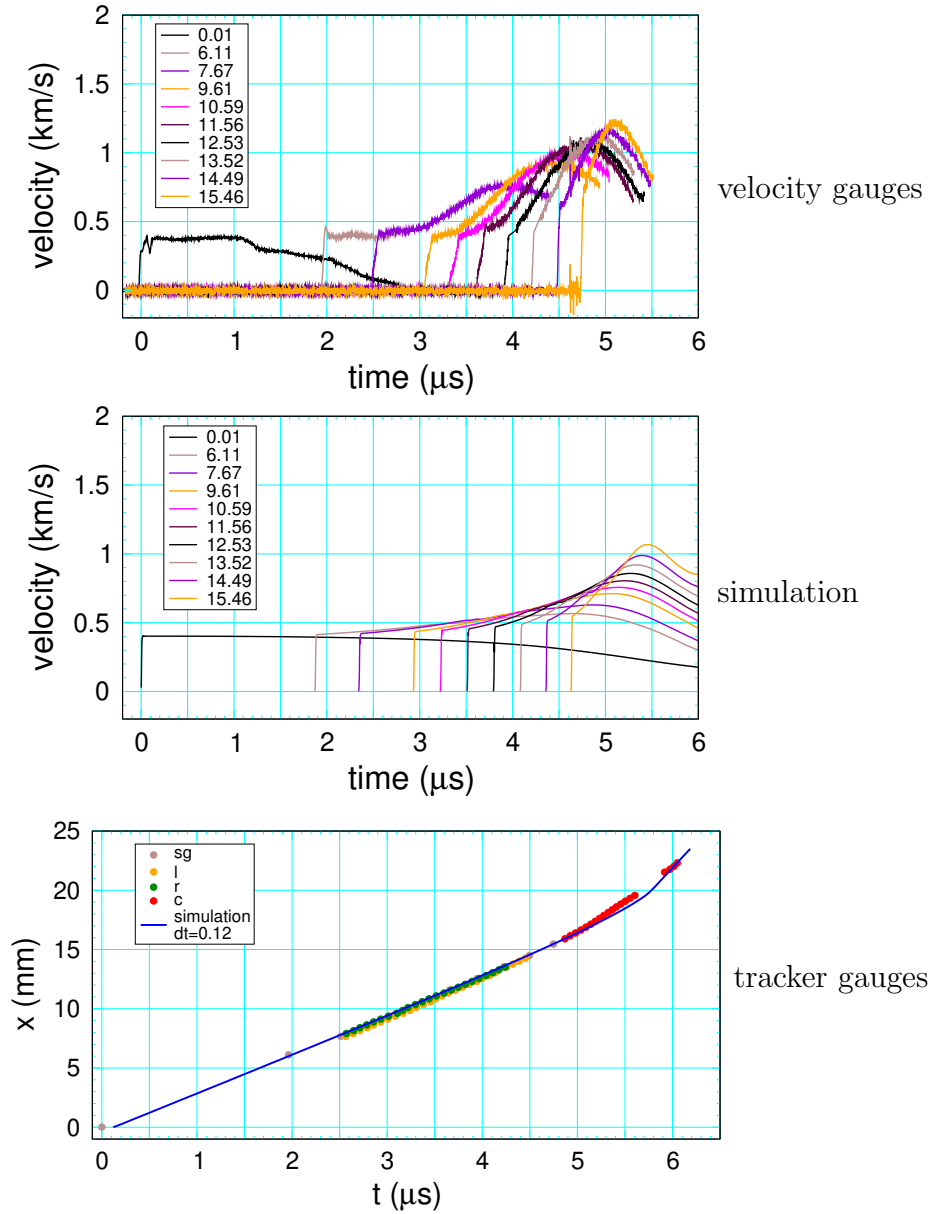
6.1 shot 1s-1675

Figure 11: Comparison for shot 1s-1675 between experimental data [Burns and Chiquete, 2020] and SURFplus model simulation. Top and middle plots for embedded velocity gauge data (legend labels gauge position in mm) and bottom plot for lead shock trajectory.

This shot did not transit to a detonation within the run distance covered by the center tracker data. In contrast, the simulation did detonate. Though the velocity gauge profiles are not that different. The local average shock velocity, shown in fig. 19, is not monotonic. It is not clear whether a transition would occur after a longer run distance. Based on the LX-07 Pop plot data, shown in fig. 10, a detonation would be expected with a slightly longer run distance than given by the Pop plot. It would be worthwhile to repeat this shot.

16

6.2 shot 1s-1674

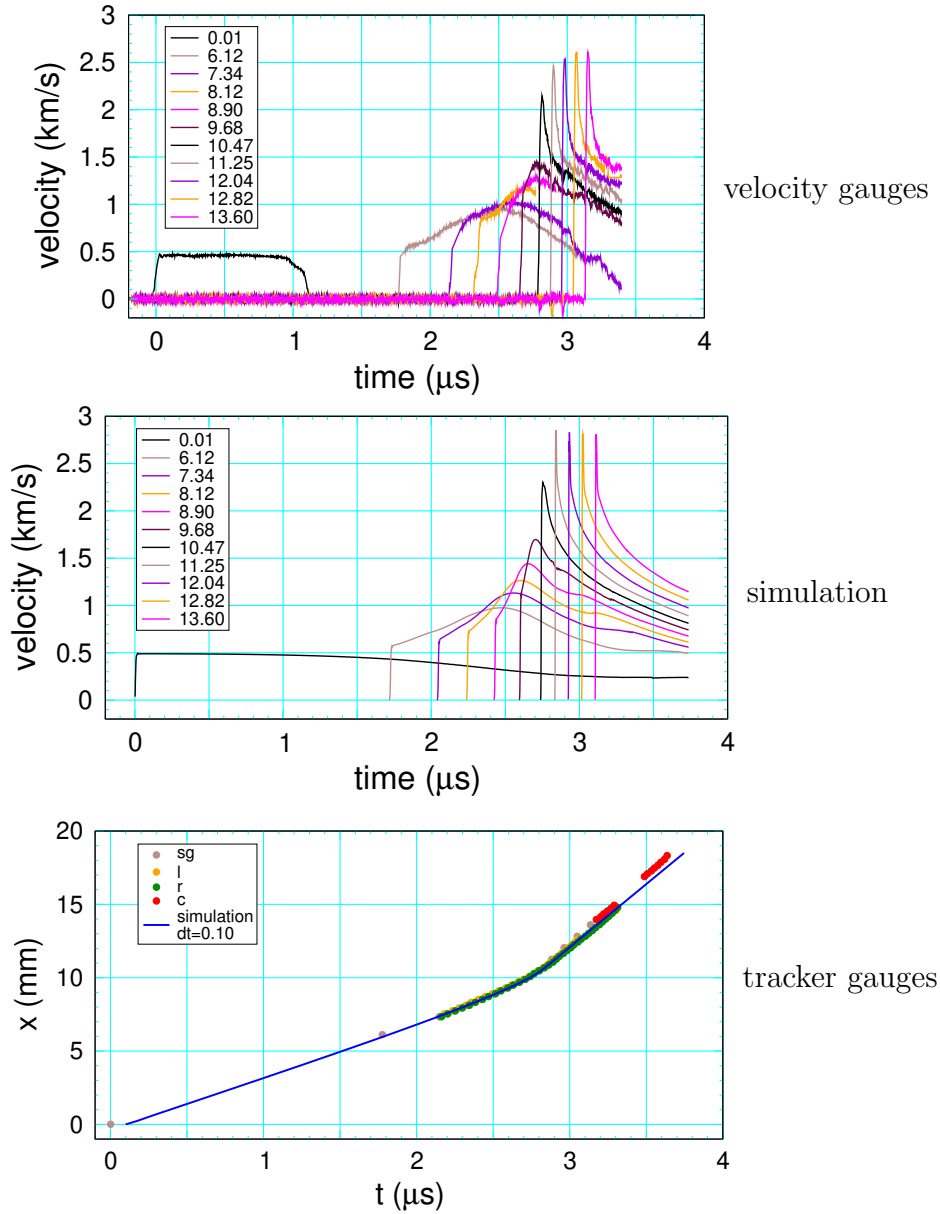

velocity gauges

simulation

tracker gauges

Figure 12: Comparison for shot 1s-1674 between experimental data [Burns and Chiquete, 2020] and SURFplus model simulation. Top and middle plots for embedded velocity gauge data (legend labels gauge position in mm) and bottom plot for lead shock trajectory.

The noise free straight lines behind the shock for some of the gauges are due to missing data points. This results in a large uncertainty in identifying the particle velocity behind the lead shock. There is also a noticeable offset in the shock positions between the center and right trackers which implies the detonation front is not planar. Moreover, after a gap in the center tracker data, the offset increases.

17

6.3 shot 1s-1684

Figure 13: Comparison for shot 1s-1684 between experimental data [Burns and Chiquete, 2020] and SURFplus model simulation. Top and middle plots for embedded velocity gauge data (legend labels gauge position in mm) and bottom plot for lead shock trajectory.

There is no data for the left and right tracker gauges. The transition to detonation lies between the position of the last velocity gauge and the first center tracker data point. After the transition, the simulation trajectory is offset from the experimental trajectory. The offset is comparable to the difference between the center and right tracker data of the previous shot (1s-1674).
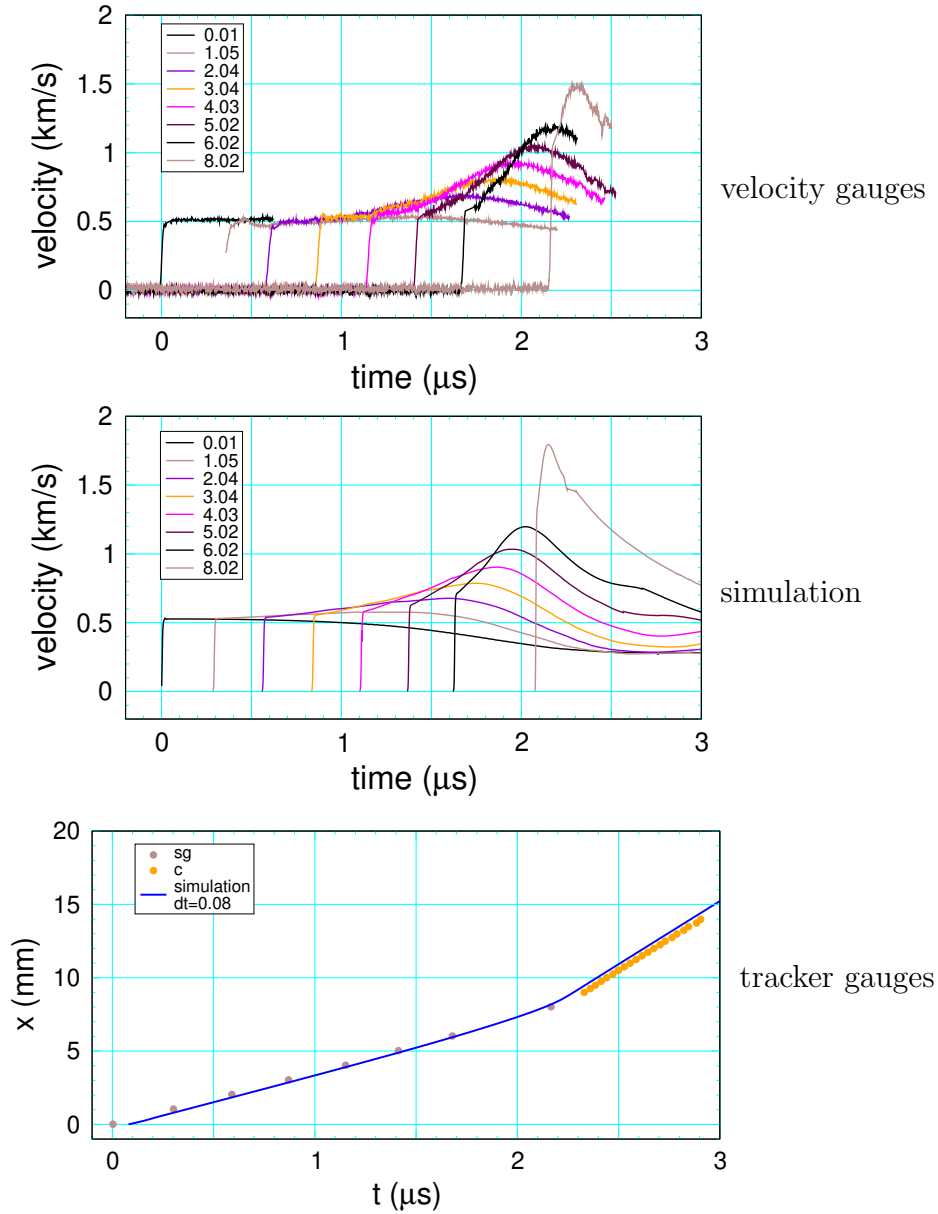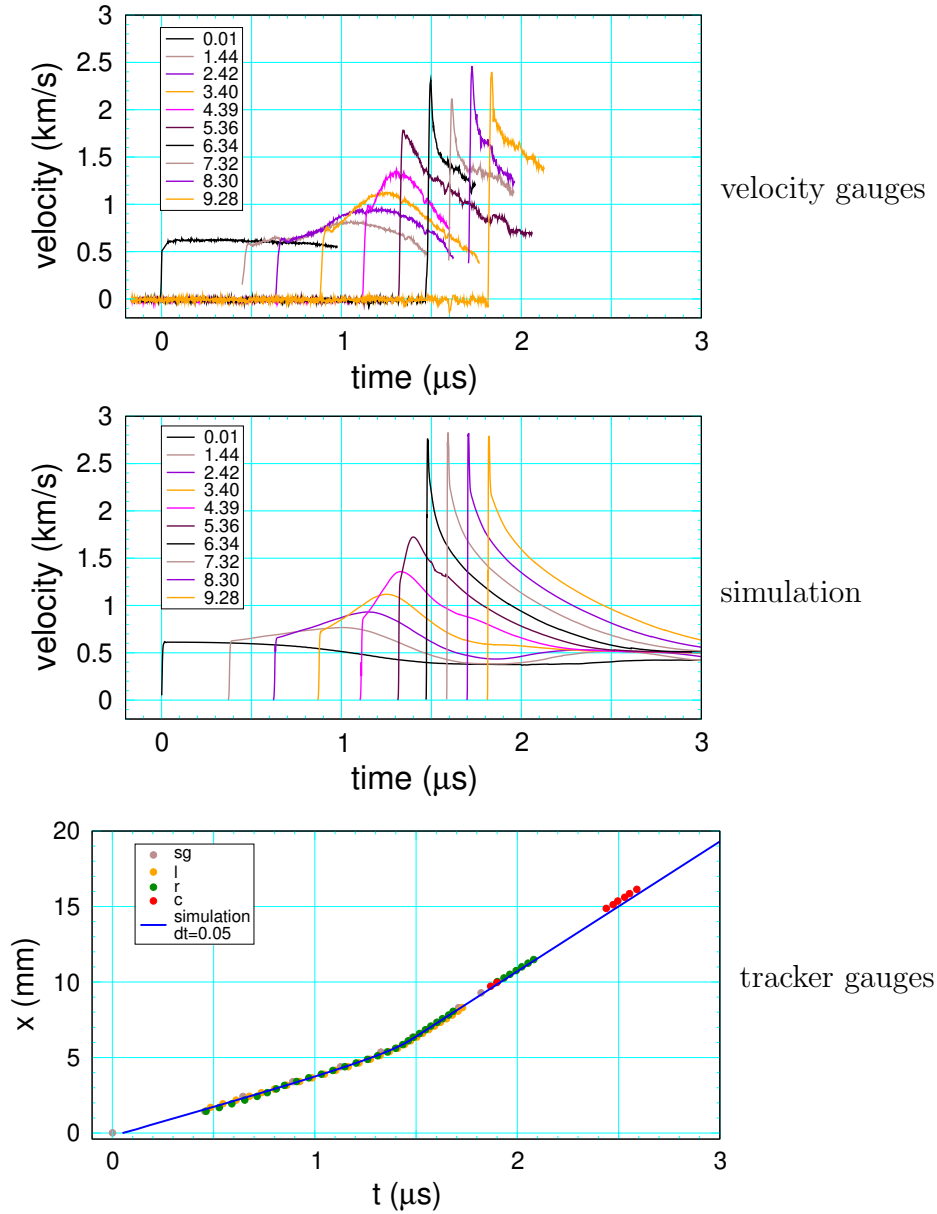
6.4   shot 1s-1673

Figure 14:   Comparison for shot 1s-1673 between experimental data [Burns and Chiquete, 2020] and SURFplus model simulation. Top and middle plots for embedded velocity gauge data (legend labels gauge position in mm) and bottom plot for lead shock trajectory.

The experimental and simulated data are in good agreement. There is a difference in the shock trajectory at late time due to an offset in the center tracker data. Without the center tracker data, the ODE fit has final shock speed D very close to D_{cj} and in agreement with the simulation. With the center tracker, D is 4.5 percent above D_{cj}; see fig. 18 and Table 3.

6.5 shot 2s-1101

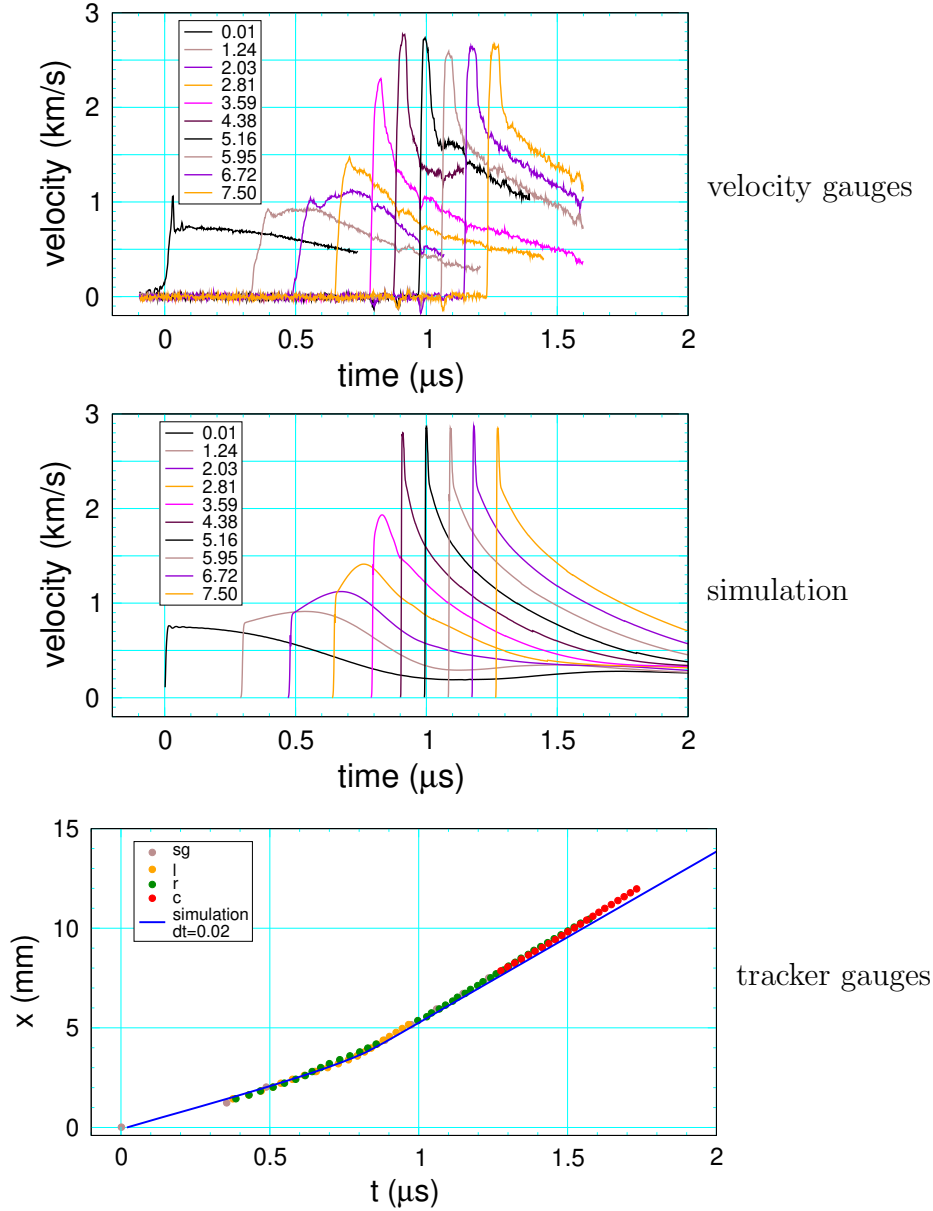

velocity gauges

simulation

tracker gauges

Figure 15: Comparison for shot 2s-1101 between experimental data [Burns and Chiquete, 2020] and SURFplus model simulation. Top and middle plots for embedded velocity gauge data (legend labels gauge position in mm) and bottom plot for lead shock trajectory.

This is only the 2-stage gas gun shot in the SDT experiment series. The data for the stirrup and early velocity gauges show the lead shock is smeared out more than usual. This affects the shape of the gauge profile; *i.e.*, distinguishing between the lead shock and the following compressive wave from the pressure increase due to reaction. The width of the detonation wave profiles are noticeably wider than for the 1-stage gas gun shots. The experimental detonation speed is 4.3 percent above D_{cj}. Consequently, after the transition to detonation, the experimental and simulated shock trajectories have different slopes.

7 Curvature effect

Propagating detonation waves are characterized by the curvature effect; detonation speed as function of front curvature, $D_n(\kappa)$. For PBX 9012, the curvature effect has been determined from the detonation front shape of rate stick experiments [Anderson et al., 2020, eq 1 & table 2]. It is used to calibrate the burn rate for the high pressure regime of a detonation wave.

For PBX 9012, the experimental $D_n(\kappa)$ curve is shown in fig. 16. We note that the magnitude of the slope $(-\mathrm{d}D_n/\mathrm{d}\kappa)$ is large and decreasing for small κ and then varies more slowly for larger κ. A fast-slow reaction is needed to fit this property of $D_n(\kappa)$. The SURFplus model is used, even though the slow rate was motivated by carbon clustering. The slow SURFplus rate parameters are flexible enough to fit the shape of the $D_n(\kappa)$ curve for small κ.

The curvature effect for the SURFplus model can be computed from the quasi-steady reaction-zone profile ODEs; see [Menikoff and Shaw, 2012, §2]. From the ODEs we find that for small κ the change in slope of the curvature effect is largely due to the shift in the sonic point from the end of the slow reaction-zone at $\kappa = 0$ to near the end of the fast reaction-zone at $\kappa \approx 0.1\,\mathrm{mm}^{-1}$, and that for $\kappa > 0.1\,\mathrm{mm}^{-1}$ the slope is determined largely by the width of the fast reaction-zone. We also find that the extrapolated SURF rate from the ignition regime to the propagating regime gives a burn rate a factor of 2 too small to obtain the very narrow reaction-zone width needed to fit the slope of the curvature effect for large κ.

To circumvent this difficulty, a partly resolved reaction-zone feature was add to the SURF model in the xRage code. This allows a controlled amount of burning to occur in the shock profile when the cell size in the reaction zone is sufficiently small. It has little effect when the cell size dominates the numerical reaction-zone width. Thus the effect of the feature is to decrease the reaction-zone width, but only when fine zoning is used. The implementation is specified in Appendix E. A small modification is also needed for the reaction-zone ODEs. Instead of initializing the ODEs to the state of a reactant shock at a specified wave speed, the ODEs are initialized to the state on the partially reacted shock locus with specified wave speed and the desired value of the reaction progress variable; see [Menikoff, 2015].
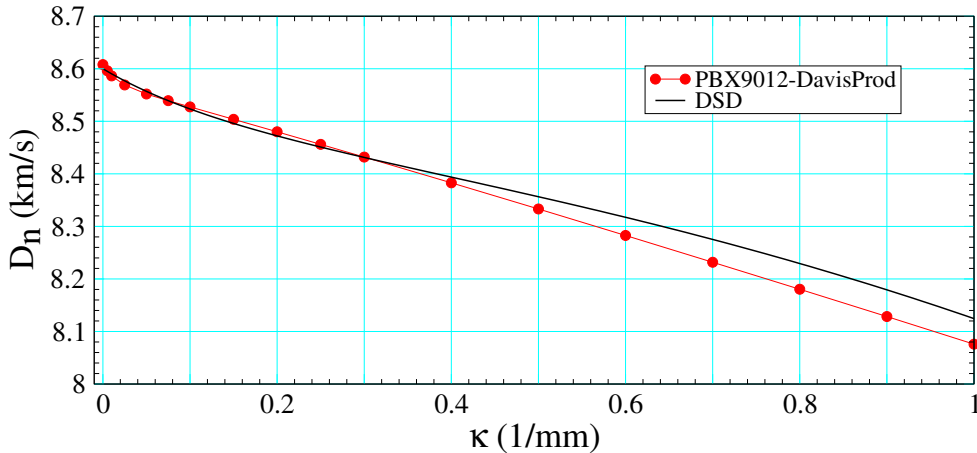

Figure 16: $D_n(\kappa)$ for PBX 9012 from SURFplus model compared to DSD fit to experiment.

A comparison of the experimental and model curvature effects is shown in fig. 16. The model is more accurate for $\kappa < 0.4\,\mathrm{mm}^{-1}$ then for larger κ. This is a deliberate trade-off as large κ typically occurs only in a boundary of an unconfined rate stick and deemed less important than small κ; see discussion of curvature effect in [Menikoff, 2019].

8   Final remarks

All HE reactive burn models are empirical. They can be no more accurate than the experimental data used to calibrate the model. For PBX 9012 there are accuracy issues with the measured reactants shock locus determined from the shock-to-detonation transition (SDT) experiments using the shock jump relation $P_s = \rho_0 u_p u_s$. In particular, the initial shock pressure inferred from the gauges is not consistent with the shock impedance match of the gas gun projectile impacting the HE target. This is important for the SDT calibration simulations since the impedance match is what determines the initial shock pressure that drives the transition.

There are two main contributors to the inaccuracy of the shock data points determined from the gauges. First, the glue layers between the gauge package and the HE. Due to compatibility issues with PBX 9012, a silicon based glue was substituted for the usual low viscosity glue. The more viscous silicon glue resulted in thicker glue layers. Moreover, the glue thickness can vary. This affects how well the particle velocity behind the lead shock can be determined. Second, is the ODE fits to the lead shock trajectory used to determine the shock speed. Though the residuals of the fits are small, the derivative or shock speed is more sensitive. Especial since the variable glue thickness gives rise to variable time offsets between the different tracker gauges. Additional experiments to accurately determine the shock locus in the range of the initial shock pressure for the shock-to-detonation transition shots would be worthwhile.

For the calibration of the burn rate in the initiation regime, the Pop plot was adjusted to use the initial shock pressure from the shock impedance match with the projectile. In addition, the run distance inferred from shock trajectory fits were corrected for 2 shots to be consistent with where the velocity gauges first showed a detonation wave. With these adjustments, simulations with calibrated model are in reasonable agreement with the SDT experiments. An exception, is the lowest pressure SDT experiment that did not transit to a detonation. This is surprising since data for LX-07, which has nearly the same composition but slightly higher initial density and less sensitive, does transit. It would be worthwhile to repeat this experiment.

The burn rate in the detonation propagation regime is calibrated to the curvature effect. Rate stick data shows that the curvature effect is very small. This requires a very large burn rate in order to have a sufficiently small reaction-zone width. Extrapolating the burn rate from the initiation regime to the propagation regime results in a reaction-zone width about a factor of 2 too small. To circumvent this difficulty, a partly resolved reaction-zone feature was added to the `xRage` code. For the SURFplus model, the numerical curvature effect decrease with the cell size. To get the detonation speed within 0.1 percent for PBX 9012, a cell size of about $5\,\mu\mathrm{m}$ is needed to sufficiently resolve the very narrow reaction zone.

Appendices

A   Stirrup gauge data

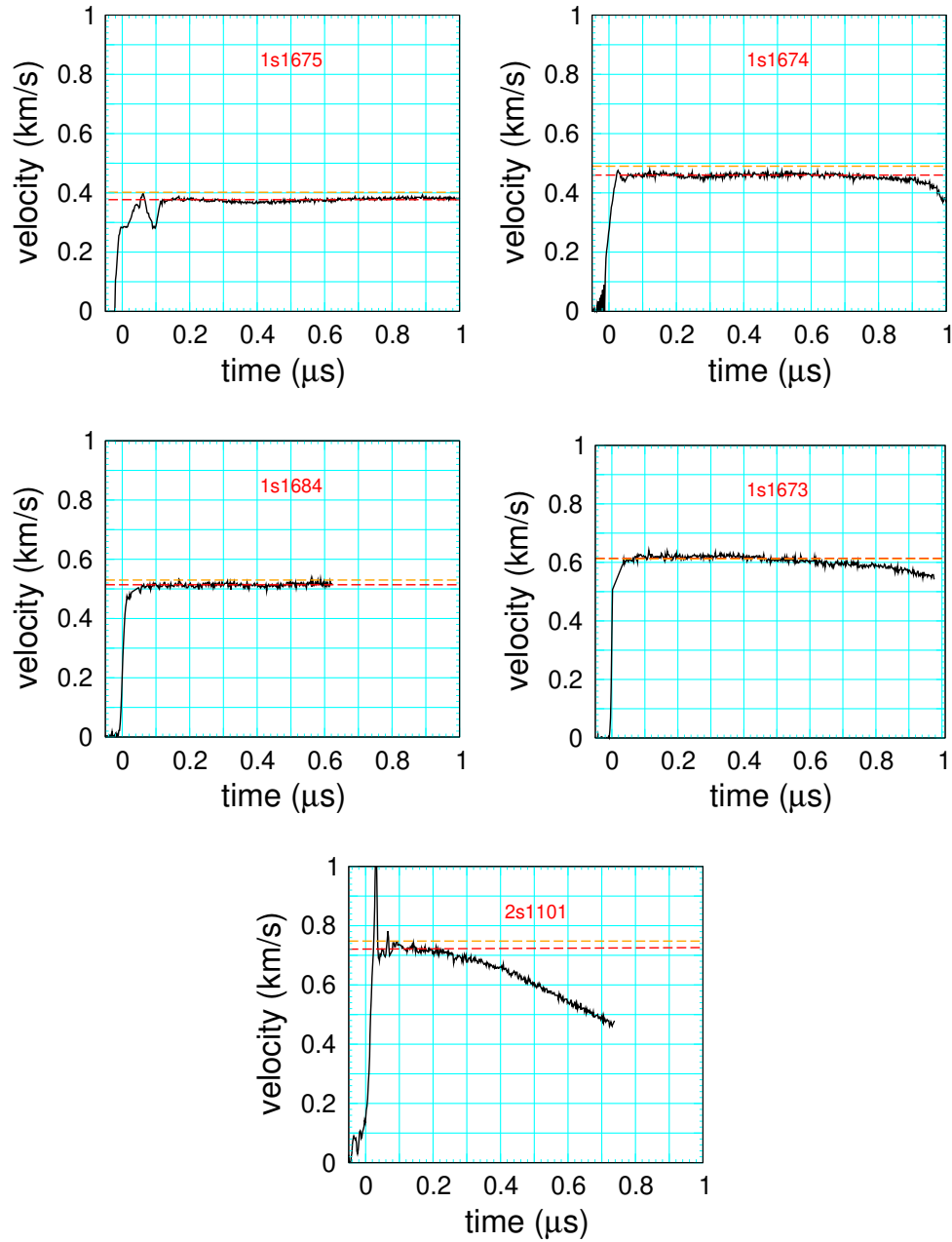
Figure 17:   Stirrup gauge velocity time histories for PBX 9012 experiments of Burns and Chiquete [2020]. Horizontal dashed red line is initial shock particle velocity from [Burns and Chiquete, 2020, table 2]. Dashed orange line is the value from the impedance match of the projectile impact using the reactants EOS parameters in [Burns and Chiquete, 2020, table 9].
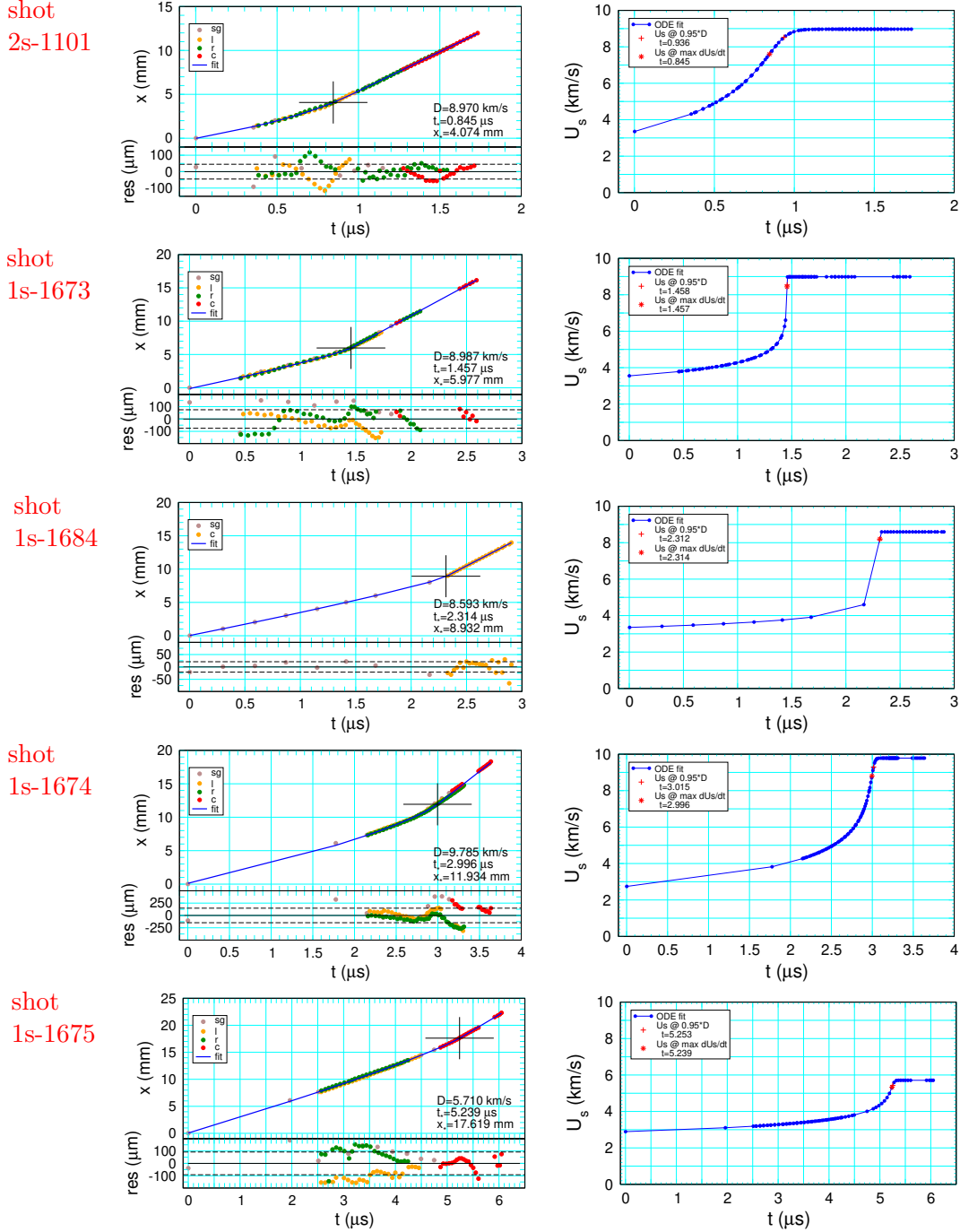
B   Tracker gauge data and ODE fits

Figure 18: Shock trajectory from tracker gauge data and ODE fits for the 5 PBX 9012 shots. Tracker gauge fits are equivalent to Burns & Chiquete's plots on small-scale database. On the left plots, cross hair indicate the point of maximum shock acceleration. Bottom of trajectory plots are the residual of the fit, $x(t) - x_{fit}(t)$, color coded by tracker gauge; sg, l, r, c for stirrup plus velocity gauges, left, right and center trackers, respectively. Dashed lines indicate ± root mean square of the residual. Right plots are the lead shock speed time history from the ODE fits. Red symbols are two transition criterion; * for point of maximum acceleration (inflection point of $U_s(t)$), and + for point at which $U_s = 0.95 * D$.

24

Table 3: ODE parameters for fits to PBX 9012 shots. RMS is the root mean square of the residual. t_* and x_* are transition point from maximum acceleration criteria. Gauges are abbreviated as s and g, for stirrup and velocity gauges, and l, r, c for left, right and center tracker gauges, respectively.

		x_0	$U_s(0)$	D	U_m	a_m	RMS	$\frac{D-D_{cj}}{D_{cj}}$	t_*	x_*
shot	gauges	mm	km/s	km/s	km/s	mm/μs^2	μm	percent	μs	mm
2s-1101	sglrc	-0.014	3.354	8.970	7.602	11.48	45	4.3	0.845	4.074
1s-1673	sglrc	-0.121	3.550	8.987	8.438	317.3	75	4.5	1.457	5.977
1s-1684	sgc[†]	0.035	3.351	8.593	8.207	4000[‡]	21	-0.8	2.314	8.932
1s-1674	sglrc	0.117	2.744	9.785	8.805	26.56	147	13.8	2.996	11.934
1s-1675	sglrc	0.052	2.893	5.710[♭]	5.333	7.49	92	-33.6	5.239	17.619

[†] no data for left and right tracker gauges

[‡] fit insensitive to large a_m due to coarse data before transition

[♭] did not transit to a detonation wave, see last remark below

Remarks:

1. The plots in fig. 18 and the lines in Table 3 are ordered by decreasing initial shock pressure, based on the projectile velocity, shock impedance match with the projectile, stirrup gauge velocity and the time-to-detonation. Yet the table shows that the initial shock velocity, parameter $U_s(0)$, is not monotonically decreasing as expected for the reactants shock locus.

2. The difference in the residuals for 2 gauges is equal to the difference in the positions of the lead shock at a fixed time; *e.g.*, $x_l(t) - x_r(t) = \text{residual}_l(t) - \text{residual}_r(t)$. For shot 1s-1674, after the transition to detonation at $t = 3.3\,\mu$s, this implies that the detonation front is curved; *i.e.*, bowed out with the center leading the left and right tracker gauges by about 0.4 mm.

3. There are some large non-constant differences in the residuals between gauges, hence differences in the shock arrival time at a given position. The differences are larger than typically associated with tilt and are likely due to variations in glue thickness on the upstream side of the gauge.

4. The local variation in the shock velocity of a tracker gauge relative to the fit is related to the slope of its residual; $U_{s,data}(t) = U_{s,fit}(t) + (\mathsf{d}/\mathsf{d}t)\text{residual}(t)$. Moreover, there are time intervals for which the slope is smoothly varying rather than having high frequencies indicative of noise. For example, shot 2s-1101 before the transition to detonation the residual slopes are $\pm 0.6\,\text{mm}/\mu$s, for the right and left trackers, respectively, over an interval of $0.15\,\mu$s corresponding to 5 data point for each tracker. The velocity difference is about 10 percent of the shock speed. Also, the slope of the center gauge well after the transition implies the detonation speed jumps from $0.5\,\text{mm}/\mu$s below to $0.5\,\text{mm}/\mu$s above D, which is already 4.3 percent higher than D_{cj}.

5. Typically, $U_s(t)$ has a steep slope in neighborhood of transition-to-detonation due to a large value of the parameter a_m. In this case, the transition point is insensitive to the transition
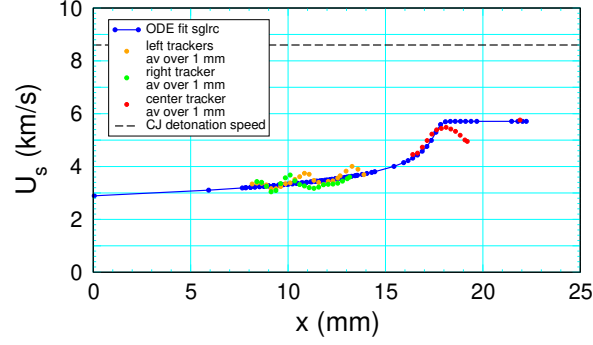
25

Figure 19: Comparison of shock velocity for shot 1s-1675 from ODE fit and local average velocity over 1 mm intervals.

criterion. Shot 2s-1101 is an exception with a significant time difference between transition criterion seen in the plot of the shock speed.

6. The final velocity parameter D can differ significantly from D_{cj}; 14 percent for shot 1s-1674.

7. The lowest pressure shot 1s-1675 has $u_s(t)$ characteristic of a transition-to-detonation, but its final velocity is 30 percent less than D_{cj}. This is misleading as the fitting form for the acceleration goes to 0 at late time, and hence forces the shock speed to go to a constant. Figure 19 compares the shock speed from the ODE fit and a local average speed from the slope of a linear fit to the tracker gauge data over 1 mm intervals. Clearly a constant final velocity is an artifact of the fitting form.

The different tracker gauges can be thought of as redundant measurements of the lead shock trajectory. It is natural to examine how the ODE fits vary for the different trackers. This is also useful for estimating what the effect on accuracy of a fit would be when data is lost for some of the tracker gauges; *e.g.*, on shot 1s-1684, there is data only for the center tracker. Moreover, if data from the center tracker is lost then the tracker data would not extent as far past the transition point. This can affect the final detonation speed and hence the transition point as will be seen later for shot 1s-1674.

B.1   Shot 2s-1101

For selected tracker data of shot 2s-1101, fig. 20 shows plots of the trajectory fits and Table 4 lists the fitting parameters.

Remarks:

1. The root mean squared residual for the fits of the left and right tracker gauges are nearly the same and slightly smaller than the fit to the combined data.

2. The shock speed time histories are significantly different. Though the final shock speed D is within a couple of percent. The transition is more abrupt for the left tracker. In addition, there is a larger variation of the transition point from the criterion that $U_s = 0.95 * D$ than for the criterion of maximum acceleration, $U_s = U_m$.
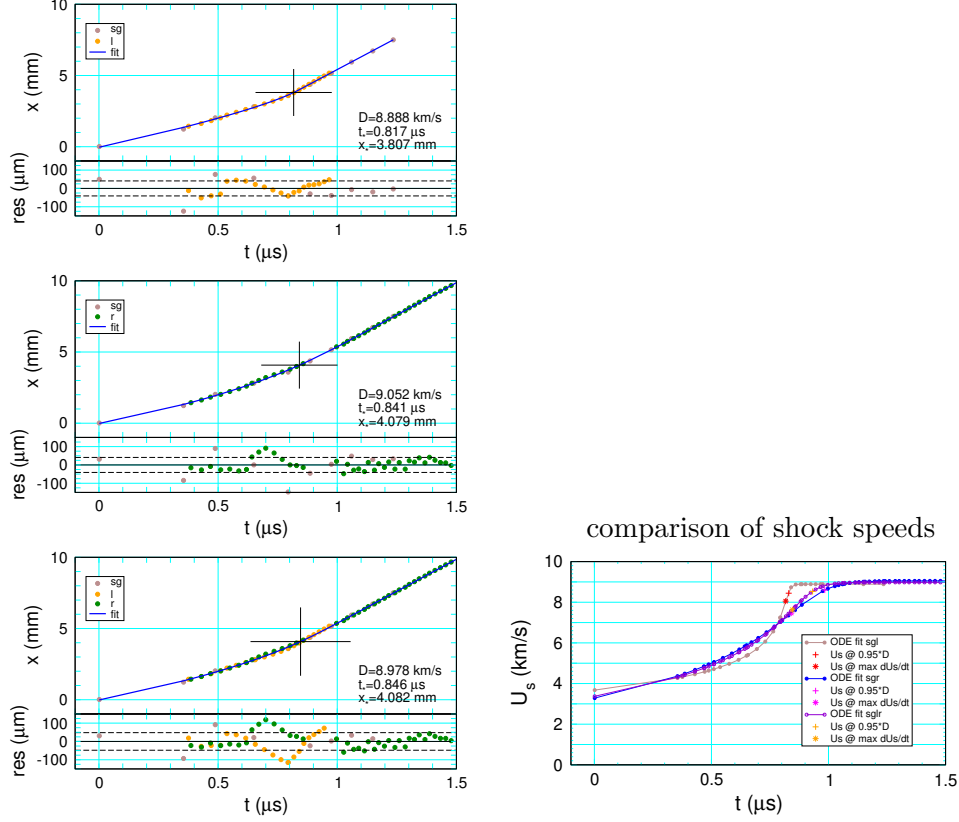
26

Figure 20: Shock trajectory fits for selected tracker gauges of shot 2s-1101, and comparison of shock speed time history, $u_s(t)$.

Table 4: ODE parameters for fits of selective trackers of shot 2s-1101. RMS is the root mean square of the residual. t_* and x_* are transition point from maximum acceleration criteria. Gauges are abbreviated as s and g, for stirrup and velocity gauges, and l, r, c for left, right and center tracker gauges, respectively.

shot	gauges	x_0 mm	$U_s(0)$ km/s	D km/s	U_m km/s	a_m mm/μs^2	RMS μm	$\frac{D-D_{cj}}{D_{cj}}$ percent	t_* μs	x_* mm
2s-1101	sglrc	-0.014	3.354	8.970	7.602	11.48	45	4.3	0.845	4.074
2s-1101	sglr	-0.017	3.372	8.978	7.634	11.86	48	4.4	0.846	4.082
2s-1101	sglr†	-0.055	3.632	8.60†	7.667	21.3	69	0.0	0.799	3.745
2s-1101	sgl	-0.036	3.676	8.888	8.053	38.4	41	3.3	0.817	3.807
2s-1101	sgr	-0.018	3.283	9.052	7.464	9.3	41	5.3	0.841	4.079

† Restricted fit with D set to D_{cj}

3. The initial shock speed $U_s(0)$ is an extrapolation from the domain of the tracker gauge data, and varies from 3.28 for the left tracker to 3.68 km/s for the right tracker; a difference of 12 percent.

4. The final detonation speed from the ODE fit (parameter D) is approximately the slope of a linear fit to the trajectory after the transition to detonation. For the combined left and right tracker data, D is 4.4 percent higher than D_{cj}.

27

To better understand the high value of D, the local shock speed from the tracker data is shown in fig. 21. It is based on a running average of the slope of a linear fit to the $x(t)$ data over 1 mm intervals. Nominally, the spacing between tracker points is 0.2 mm. Hence, a 1 mm interval has 4 or 5 data points for each of the left and right trackers. The local shock speed is noisy due to the uncertainty in the data points, and is compatible with the variation of the slope of the residuals. By construction the shock speed from the ODE fit is smooth and averages out the short wavelength variations. There is some indication at late time that the shock speed approaches D_{cj}. But this maybe a statistical fluctuation from the uncertainty in the data points; estimated to be $\sigma_x = 0.018$ mm and $\sigma_t = 0.012\,\mu$s in [Burns and Chiquete, 2020, table VII].

Figure 22 shows the effect on the fit to the trajectory and shock speed when D is constrained to be D_{cj}. The trajectories are nearly indistinguishable by eye, though the RMS residual increases by 44 percent. There is a notable difference in the shock speed time history that affects the transition point and the initial shock speed. Table 5 gives the fitting parameters and their standard deviations with the other parameters held fixed. We note that the difference in D is $7.4\,\sigma_D$, which would be improbable if D is a Gaussian random variable. This illustrates that larger correlated changes in the fitting parameters can have a small effect on the fit; see Press et al. [1986, sec. 14.5] for a discussion of the covariance matrix of a least squared fit. However the derivative or shock speed is much more sensitive than the trajectory, especially in the region of the transition to detonation. There is also an 8 percent difference in the initial shock speed.
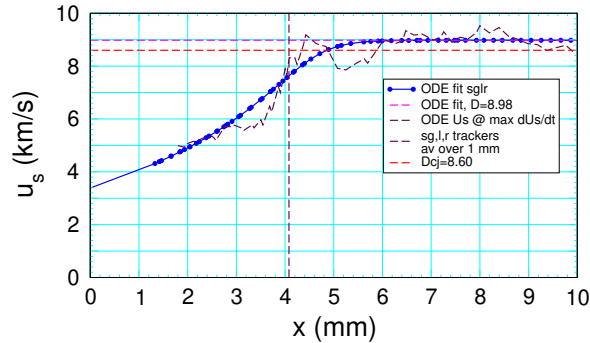

Figure 21: Local and ODE fit shock speed for shot 2s-1101 with combined left and right tracker data.
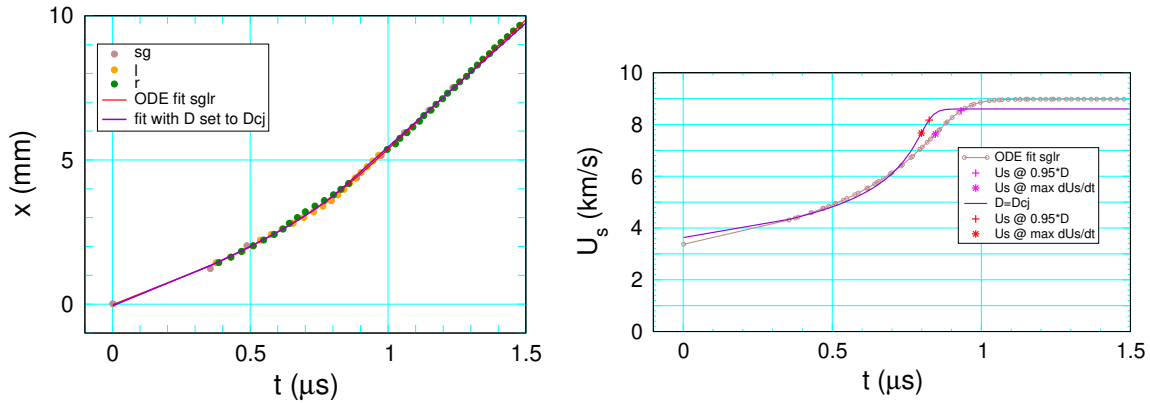

Figure 22: Comparison of shock trajectory and shock speed for fits of shot 2s-1101 for left and right tracker gauges with and without the final shock speed parameter D constrained to be D_{cj}.

28

Table 5: Fit to shot 2s-1101 for gauges sglr with and without D constrained to be D_{cj}. σ is standard deviation of each fitting parameter with the other parameters held fixed.

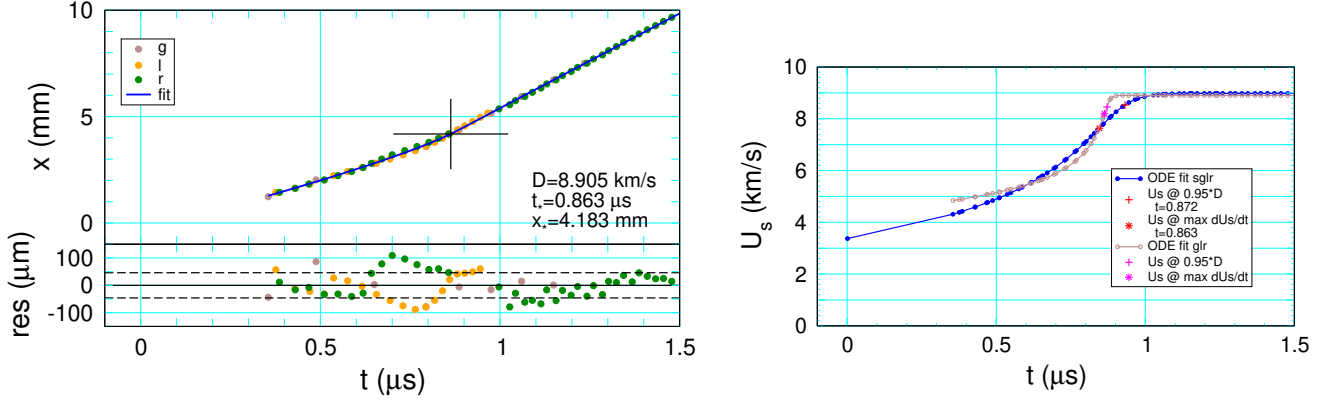|	x_0	$U_s(0)$	D	U_m	a_m	RMS	$\frac{D-D_{cj}}{D_{cj}}$	t_*	x_*
	mm	km/s	km/s	km/s	mm/μs^2	μm	percent	μs	mm
D parameter	-0.017	3.372	8.978	7.634	11.86	48	4.4	0.846	4.082
σ	0.046	0.154	0.051	0.116	1.5				
D set to D_{cj}	-0.055	3.632	8.60	7.667	21.3	69	0.0	0.799	3.745

Figure 23: Comparison of shock trajectory and shock speed for fits of shot 2s-1101 with/without stirrup gauge.

A related issue for the accuracy of the shock speed is that the 3 fitting parameters for the shock acceleration (D, D_m and a_m) involve quantities quantities near the final shock speed. Extrapolation of the fitting form to lower shock speeds is potentially error prone.

There is a large gap between the position of the stirrup gauge and the start of the velocity and tracker gauges. Figure 23 shows the fit with the stirrup gauge data point excluded. In the region of the tracker data there is very little difference in the trajectory due to correlated changes in the fitting parameters. But there is a significant difference in $U_s(t)$. In particular, the transition to detonation is much sharper and less sensitive to the transition criterion, which is similar to the plots of the other shots shown in fig. 18.

This example illustrates an issue with global fits that are lacking a strong physical motivation. One expects the velocity to depend on local data and be insensitive to data far away in time. Yet the one point at the origin has a large effect on the velocity in the neighborhood of the transition point.

B.2 Shot 1s-1674

Another notable example in which the choice of trackers significantly affects D and the transition point to detonation occurs for shot 1s1674; see fig. 24 and Table 6. For the three cases (left, right and combined left and right tracker data), the parameter D ranges from 8.27 to 8.63 km/s.

For all the data (including the center gauge), fig. 18 and Table 3 show a much larger D of 9.78 km/s and a transition time about 0.15 μs larger.

With the center tracker, the value of D is 14 percent above D_{cj}, which is unreasonably large. In addition, the RMS residual is 3 times larger than the fit without the center tracker. This anomalous behavior of the fit is due to a time shift with the center gauge data being earlier than the left and right gauge data. This affects the average slope of the trajectory after the transition-to-detonation. The earlier time of the center tracker may be due to the detonation front being bowed out with the center leading the left and right gauge positions by 0.4 mm.
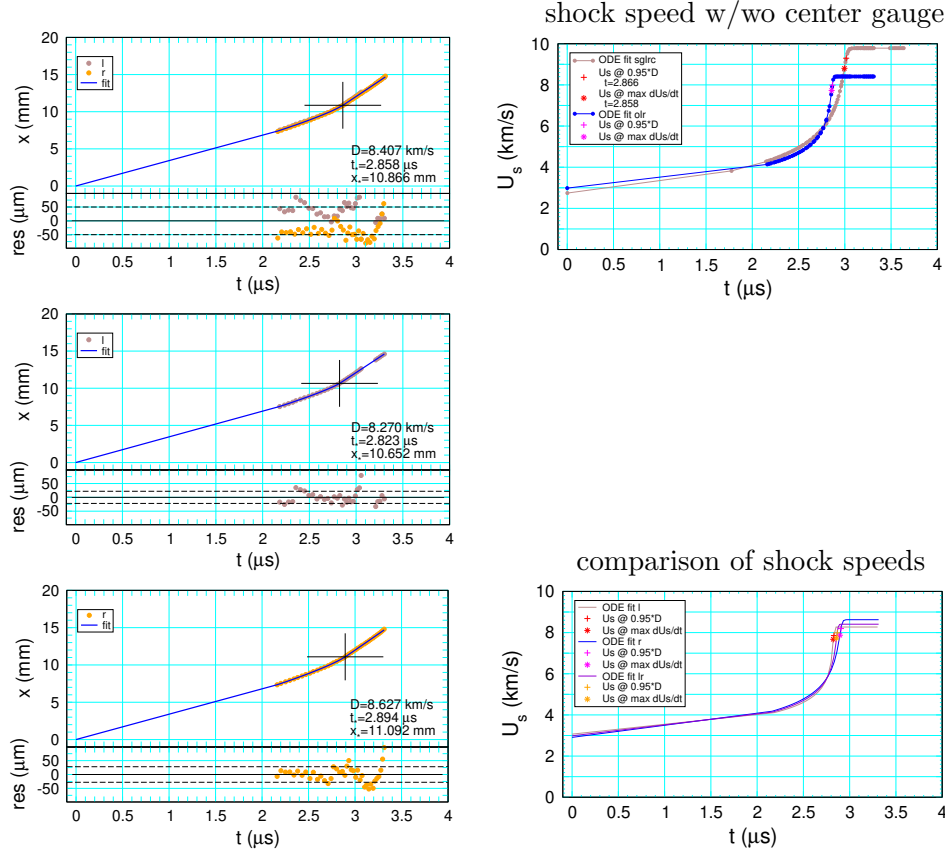

Figure 24: Shock trajectory fits for selected tracker gauges of shot 1s-1674, and comparison of shock speed time history, $u_s(t)$.

Table 6: ODE parameters for fits of selective trackers of shot 1s-1674. RMS is the root mean square of the residual. t_* and x_* are transition point from maximum acceleration criteria. Gauges are abbreviated as s and g, for stirrup and velocity gauges, o for origin, and l, r, c for left, right and center tracker gauges, respectively.

shot	gauges	x_0 mm	$U_s(0)$ km/s	D km/s	U_m km/s	a_m mm/μs^2	RMS μm	$\frac{D-D_{cj}}{D_{cj}}$ percent	t_* μs	x_* mm
1s-1674	sglrc	0.117	2.744	9.785	8.805	26.6	147	13.8	2.996	11.934
1s-1674	olr	0.000	2.984	8.407	7.730	38.5	50	-2.2	2.858	10.866
1s-1674	ol	-0.002	3.066	8.270	7.674	64.0	22	-3.8	2.823	10.652
1s-1674	or	0.002	2.908	8.627	7.870	28.9	28	0.3	2.894	11.092

C   EOS parameters for PBX 9012

xRage teos.in file parameters for PBX 9012 EOS

C.1   Davis reactants EOS

Davis reactants parameters from [Burns and Chiquete, 2020, table IX].

```
matid($mat)     = 90127          ! table number
matident($mat)  = "PBX9012-reactants"
eostype($mat)   = 14             ! Davis reactants EOS
matdef( $mat,2) = 1e10           ! Pscale, 1GPa
matdef( 3,$mat) = 1.845          ! rho0
matdef( 4,$mat) = 0.0            ! e0
matdef( 5,$mat) = 0.0            ! P0
matdef( 6,$mat) = 297.           ! T0, K
matdef( 7,$mat) = 1.99           ! A, km/s
matdef( 8,$mat) = 3.261128       ! B
matdef( 9,$mat) = 2.071103       ! C
matdef(10,$mat) = 0.6185         ! Gamma0
matdef(11,$mat) = 0.0            ! Z
matdef(1$mat,2) = 0.623          ! alpha
matdef(13,$mat) = 1.170e-3       ! Cv, MJ/kg/K
```

C.2 Products EOS

The HE model calibration for the products uses Davis products EOS with parameters from
[Anderson et al., 2020, table 6] listed below.

```
$mat = ($mat+1)
matid($mat)      = 90129          ! table number
matident($mat)  = "PBX9012-products"
eostype($mat)   = 15              ! Davis products EOS
matdef( 2,$mat) = 1e10            ! Pscale, 1GPa
matdef( 3,$mat) = 1.845           ! rho0
matdef( 4,$mat) = (5.649)         ! e0=Edet
matdef( 5,$mat) = 0.0             ! P0
matdef( 6,$mat) = 0.9688          ! Vc
matdef( 7,$mat) = 1.4076          ! Pc
matdef( 8,$mat) = 0.0             ! Tc, replace with default

matdef( 9,$mat) = 0.9125          ! a
matdef(10,$mat) = 0.7317          ! b
matdef(11,$mat) = 2.1602          ! n
matdef(12,$mat) = 1.3820          ! k
matdef(13,$mat) = 1.150e-3        ! Cv, MJ/kg/K
```

C.3 Materials input

Material section of `xRage` input file

```
include "units.HE"                        ! standard units conversion factors
!
! PBX9012
!
! HE reactants
matident(matid_r) = "PBX9012-rectants"
matdef(1,matid_r) = 90127                 ! Davis reactants
!
sizemat(matid_r) = (0.050*$mm)
sizebnd(matid_r) = (0.050*$mm)

! HE products
matident(matid_p) = "PBX9012-products"
matdef(1,matid_p) = 90129                 ! Davis products
!
sizemat(matid_p) = (0.050*$mm)
sizebnd(matid_p) = (0.050*$mm)
```

D SURFplus rate parameters for PBX 9012

The fitting forms for the SURF and SURFplus rates are specified in the xRage users manual. SURF rate parameters for PBX 9012 (fitting form 4) along with SURFplus carbon clustering parameters are given below.

```
he_model(1)       = 7                   ! SURFplus model
he_unreacted(1)   = matid_r             ! reactants
he_reacted(1)     = matid_p             ! products


he_specific_energy(1) = (0*$MJ_kg)      ! fine tune CJ state
he_dtpct(1)       = 0.27                ! cfl number of detonation wave
he_zone_size(1)   = (0.012*$mm)         ! refine to zone_size
he_w_cutoff(1)    = 0                   ! burn fraction cutoff
he_refine_dw(1)   = 0.0001              ! dw for refinement


he_surf_Pburn(1) = (2*$GPa)             ! burn threshold for CJ detonation
he_pscale(1)      = (1*$GPa)            ! pressure scale for rate
he_tscale(1)      = (1*$microsec)       ! time     scale for rate
!
! fitting form 4
he_surf_P0(1)     =  1.35               ! dimensionless (p0/pscale)
he_surf_Plow(1)   =  5                  ! dimensionless (plow/pscale)
he_surf_P1(1)     = 45.0                ! dimensionless (p1/pscale)
he_surf_Phigh(1) = 60.0                 ! dimensionless (phigh/pscale)
!
he_surf_C(1)      = 0.0192              ! dimensionless (c/tscale)
he_surf_fn(1)     = 2.35                ! dimensionless
!
he_surf_n(1)      =  1.2                ! dimensionless
he_surf_nhi(1)    =  1.2                ! dimensionless
he_surf_s1(1)     =  2.0                ! dimensionless
!
! Carbon clustering
he_surfplus_Q(1)   = 0.35               ! dimensionless (q/(pscale*g/cc))
he_surfplus_Nratio(1) = 20              ! dimensionless
he_surfplus_t1(1) = 0.001               ! dimensionless (t1/tscale)
he_surfplus_t2(1) = 0.060               ! dimensionless (t2/tscale)
he_surfplus_h1(1) = 0.001               ! dimensionless
he_surfplus_h2(1) = 0.95                ! dimensionless
!
! partly resolved reaction zone
he_surf_s0_max(1)  = 0.828              ! lambda = 0.5
he_surf_Phs_min(1) = 25
he_surf_Phs_max(1) = 32
```

E   SURF rate for partly resolved reaction-zone

A new feature was added to the SURF rate model. It is aimed at decreasing the reaction-zone width of a propagating detonation wave when a fine mesh is used. This is useful for decreasing the curvature effect when the extrapolated burn rate from the ignition regime is not sufficiently large. On coarse meshes that do not resolve the reaction, the feature has little effect.

The feature is implemented with a pseudo-rate for burning in the lead shock profile at high pressures comparable to the CJ pressure. The amount of burning in the shock profile is specified by the reaction progress variable behind the shock, λ_s. In effect, the reaction-zone profile for a detonation wave starts at a point on the partially burned detonation locus λ_s instead of the von Neumann spike of the reactants shock. This is referred to as a partly resolved reaction-zone; see for example [Bdzil and Davis, 1975].

Heuristically, one can think of pore collapse by a sufficiently strong shock heating a volume of HE around the pore to a sufficiently high temperatures that the burning occurs during the late stage of pore collapse. We also note that the model reaction-zone width needed to fit the curvature effect can be smaller than the average grain size of a PBX. This implies that the assumption of a homogeneous reactant HE breaks down, and there can be fluctuations in the lead shock pressure of a detonation wave as it passes over the material heterogeneities. This can lead to a lower average lead shock pressure than the VN spike pressure. For the same detonation speed, the point on a partially burned detonation locus also has a lower pressure than the VN spike.

Burning in the shock profile is simple to implement in the SURF model due to its use of a lead shock detector. The shock is determined to be passing through a cell when its Hugoniot function first becomes positive. To reduce noise, burning is started in the shock profile when the cell pressure is above a threshold P_{burn}. Burning occurs by calculating the burn rate and updating the scaled reaction progress using Eq. (2b),

$$s(t + \Delta t) = s(t) + \text{rate}(p_s, p) * \Delta t \ . \tag{3}$$

The shock pressure variable p_s is increasing until the shock is detected. Before the shock is detected, $\text{rate}(p_s, p)$ is small. For a small cell size, Δt is small and there is little burning in the few time steps until the shock is detected; *i.e.*, little burning in the shock profile.

To implement a partly burned reaction zone, after the update in Eq. (3), a pseudo rate is added for the shock pressure variable in the interval $p_{hsmin} < p_s < p_{hsmax}$ by setting the reaction progress variable to $s = \max(s, s_0(p_s))$ where

$$s_0(p_s) = (1 - exp(-x(p_s) ** 2)) * s_{0max} \ , \tag{4}$$

$$x(p_s) = 2 * (p_s - p_{hsmin})/(p_{hsmax} - p_{hsmin}) \ , \tag{5}$$

and s_{0max}, p_{hsmin} and p_{hsmax} are model parameters with s_{0max} being the total amount of burning in the shock profile of a strong shock; $p_s > p_{hsmax}$. With p_{hsmin} near but less than p_{cj}, the additional burning only affects the high pressure detonation wave regime.

The pseudo rate is similar to programmed burn. However, the burning in the shock profile is incomplete and the reaction zone subsonic. Consequently, the feedback between the lead shock wave and the reaction wave is not lost. This is important for stability of a detonation wave.

Acknowledgement

References

E. K. Anderson, S. Chiquete, S. I. Jackson, R. I. Chicas, and M. Short. Detonation performance experiments and modeling for the HMX-based high explosive PBX 9012. part of C2 L2 Milestone 7098, September 2020.

J. B. Bdzil. Fluid Mechanics of an Obliquely Mounted MIV Gauge. Technical report, Los Alamos National Lab., March 2018. LA-UR-18-22397.

J. B. Bdzil and W. C. Davis. Time-dependent detonation. Technical Report LA-5926-MS, Los Alamos National Lab., 1975. URL http://permalink.lanl.gov/object/tr?what=info:lanl-repo/lareport/LA-05926-MS.

M. J. Burns and C. Chiquete. Shock initiation of the HMX-based explosive PBX 9012: Experiments, uncertainty analysis, and unreacted equation-of-state. *J. Appl. Phys.*, 127:215107, 2020. URL https://doi.org/10.1063/1.5144686.

T. R. Gibbs and A. Popolato, editors. *LASL Explosive Property Data*. Univ. of Calif. Press, 1980. URL http://lib-www.lanl.gov/ladcdmp/epro.pdf.

L. G. Green, R. J. Wasley, and P. E. Kramer. Shock initiation of LX-07-2 and LX-10-0. Technical report, Lawrence Livermore National Lab., April 1970. UCRL-50851, https://doi.org/10.2172/4105914.

L. G. Hill and R. L. Gustavsen. On the characterization and mechanisms of shock initiation in heterogeneous explosives. In *Proceeding of the Twelfth International Symposium on Detonation*, pages 975–987, 2002.

S. I. Jackson, E. K. Anderson, S. Chiquete, and R. I. Chicas. Data Summary of Test 8-2172. LANL OUO memo, July 2020.

R. Menikoff. Detonation wave profile. Technical Report LA-UR-15-29498rev1, Los Alamos National Lab., 2015. URL http://www.osti.gov/scitech/servlets/purl/1229720.

R. Menikoff. SURFplus model calibration for PBX 9502. Technical Report LA-UR-17-31015, Los Alamos National Lab., 2017. URL https://www.osti.gov/scitech/servlets/purl/1412839.

R. Menikoff. Accuracy of high explosive data used for reactive burn model calibration. Technical Report LA-UR-19-32062rev1, Los Alamos National Lab., 2019. URL https://doi.org/10.2172/1578002.

R. Menikoff. xRage simulations of magnetic velocity gauges used in gas gun shock initiation experiments. Technical Report LA-UR-21-21769, Los Alamos National Lab., 2021a. URL https://doi.org/10.2172/1766987.

R. Menikoff. Magnetic velocity gauges: Effects of misalignment. Technical Report LA-UR-21-22095, Los Alamos National Lab., 2021b. URL https://doi.org/10.2172/1768460.

R. Menikoff and M. S. Shaw. The SURF model and the curvature effect for PBX 9502. *Combustion Theory and Modelling*, 16:1140–1169, 2012. URL http://dx.doi.org/10.1080/13647830.2012.713994.

W. H. Press, S. A. Teukolsky, W. T. Vetterling, and B. P. Flannery. *Numerical Recipes*. Cambridge University Press, 1986. URL http://numerical.recipes/book/book.html.

K. S. Vandersall, C. M. Tarver, F. Garcia, and S. K. Chidester. On the low pressure shock initiation of octahydro-1,3,5,7-tetranito-1,3,5,7-tetrazocine based plastic bonded explosives. *J. Appl. Phys.*, 107:094906, 2010. URL http://dx.doi.org/10.1063/1.3407570.